Accepted and scheduled for publication in *The Astrophysical Journal*, for the ApJ April 20, 2013, v 767, 2nd issue

Spectral state evolution of 4U 1820-30: the stability of the spectral index of Comptonization tail

Lev Titarchuk[1], Elena Seifina[2] and Filippo Frontera[3]

ABSTRACT

We analyze the X-ray spectra and their timing properties of the compact X-ray binary 4U 1820-30. We establish spectral transitions in this source seen with *Beppo*SAX and the *Rossi* X-ray Timing Explorer (*RXTE*). During the *RXTE* observations (1996 – 2009), the source were approximately $\sim 75\%$ of its time in the soft state making the *lower banana* and *upper banana* transitions combined with long-term *low-high state* transitions. We reveal that all of the X-ray spectra of 4U 1820-30 are fit by a composition of a thermal (blackbody) component, a Comptonization component (COMPTB) and a *Gaussian*-line component. Thus using this spectral analysis we find that the photon power-law index Γ of the Comptonization component is almost unchangeable ($\Gamma \sim 2$) while the electron temperature kT_e changes from 2.9 to 21 keV during these spectral events. We also establish that for these spectral events the normalization of *COMPTB* component (which is proportional to mass accretion rate $\dot{M}$) increases by factor 8 when kT_e decreases from 21 keV to 2.9 keV. Before this index stability effect was also found analyzing X-ray data for *Z*-source GX 340+0 and for *atolls*, 4U 1728-34, GX 3+1. Thus, we can *suggest* that this spectral stability property is a spectral signature of an accreting neutron star source. On the other hand in a black hole binary Γ monotonically increases with $\dot{M}$ and ultimately its value saturates at large $\dot{M}$.

Subject headings: accretion, accretion disks—black hole physics—stars:individual (4U 1820-30):radiation mechanisms: nonthermal—physical data and processes

[1]Dipartimento di Fisica, Università di Ferrara, Via Saragat 1, I-44122 Ferrara, Italy, email:titarchuk@fe.infn.it; George Mason University Fairfax, VA 22030; Goddard Space Flight Center, NASA, code 663, Greenbelt MD 20770, USA; email:lev@milkyway.gsfc.nasa.gov, USA

[2]Moscow M.V. Lomonosov State University/Sternberg Astronomical Institute, Universitetsky Prospect 13, Moscow, 119992, Russia; seif@sai.msu.ru

[3]Dipartimento di Fisica, Università di Ferrara, Via Saragat 1, I-44122 Ferrara, Italy, email:frontera@fe.infn.it

1. Introduction

Accreting neutron stars (NS) can be observationally classified using a color-color diagram (CCD) into two distinct categories, *atoll* and *Z* sources, based on their different CCD forms when the source undergoes the spectral and luminosity changes. Along with this phenomenological difference between *atolls* and *Z*-sources in terms of the CCD there are important X-ray spectral and timing characteristics, which are essentially different for these types of NS low mass X-ray binaries (LMXB). The main observational difference between these types is the specific range of luminosity changes. The *atolls* are observed when their luminosity changes from 0.01 up to 0.5 of the Eddington limit $L_{\rm Edd}$ (see Christian & Swank 1997; Ford et al. 2000) while *Z*-sources are seen when the resulting luminosity is near Eddington regime (e.g. Seifina, Titarchuk & Frontera 2013). In this Paper we present our analysis of *peculiar atoll* 4U 1820-30, which is a *bright atoll* source in terms of its luminosity and, at the same time, it is a *typical atoll* source in terms of timing evolution. On the other hand, during bright phase 4U 1820-30 is as bright as a subclass of persistent bright *atolls* (GX 13+1,GX 9+1, GX 9+9 and GX 3+1), but 4U 1820-30 shows larger range of luminosity and demonstrates all states in terms of CCD (from the *island* to *banana* states), whereas these aforementioned bright *atolls* are only seen in the banana state (e.g. Hasinger & van der Klis 1989).

Furthermore, 4U 1820-30 has a maximal luminosity about 0.5 of $L_{\rm Edd}$ and thus it adjoins to *Z* source luminosity range. Also 4U 1820-30 shows Type-I X-ray bursts and characteristic timing features as a typical *atoll* demonstrating an evolution of band-limited noise (BLN), very low frequency noise (VLFN) components and low frequency quasi-periodic oscillations (LFQPOs) (in 20-40 Hz range) when it evolves from the *banana* to *island* states. However, opposite to the other *atolls*, 4U 1820-30 exhibits LFQPOs with frequencies near 6 Hz during the *banana* state (Wijnands, van der Klis, & Rijkhorst 1999; also see Sect. 6.2 in this Paper), which are usually seen in *Z*-sources during the Normal branch. Thus, 4U 1820-30 combines properties of ordinary and bright *atolls* and *Z*-sources in terms of timing and spectral evolution, luminosity and detection of 6 Hz QPO.

4U 1820-30 is a LMXB observed at 0.66" from the center of the NGC 6624 cluster. Grindlay et al. (1976) were the first who identified this source as a Type-I X-ray burst. Kuulkers et al. (2003) estimated the distance $d = 7.6 \pm 0.4$ kpc to 4U 1820-30 assuming that the peak luminosity equals to $L_{\rm Edd}$ for He burst atmosphere. Vacca, Lewin & van Paradijs (1986) estimate the distance to 4U 1820-30 as 6.4±0.6 kpc using the analysis of UV diagrams for NGC 6624. Rappaport et al. (1987) find that the binary system comprises of a He white dwarf of mass of 0.06±0.08 $M_\odot$ and NS, [with a mass later evaluated by Shaposhnikov & Titarchuk (2004) as ∼1.3 $M_\odot$], orbiting at the period of 11.4 minutes (Stella et al. 1987).

Hasinger & van der Klis (1989) classify 4U 1820-30 as an *atoll* source. Priedhorsky & Terrell (1984), Simon (2003) and Wen et al. (2006) find that the flux varies between the soft and the hard states (*banana* and *island* ones respectively) are quasi-periodic with period at ∼170 d and these flux variations have been suggested related to tidal effects of a remote third star [Chou & Grindlay (2001) and Zdziarski et al. (2007)]. *RXTE* observations revealed 4U 1820-30 as a prominent source of kilohertz quasi-periodic oscillations (kHz QPO) (Smale 1997). X-ray bursts are only observed at low fluxes [e.g. Clark et al. (1977)]. Furthermore, Cornelisse et al. (2003) and Zhang et al. (1998) find that the observed kHz QPOs correlate with the flux which probably suggests that these variations are because of a luminosity change caused by change of mass accretion rate.

Strohmayer & Bildsten (2004) established that the short (∼10 – 15 s) Type-I outbursts are because of the unstable thermonuclear burning of mixture of hydrogen and helium at the NS atmosphere bottom. SAS-3 observations showed strong evidence that X-ray bursts can only occur in its low-intensity state (Clark et al. 1977). All bursts observed from 4U 1820-30 indicate that a photosphere expends with an increase of a photospheric radius by a factor of 20. Such an expansion leads to strong softening of the resulting spectrum (see e.g. Strohmayer & Bildsten 2004). Moreover, a several hour long "superbursts" was observed from 4U 1820-30 on September 9, 1999. It is now understood that superbursts can be caused by the burning in the carbon ashes produced by Type-I bursts (Strohmayer & Brown 2002).

Einstein, EXOSAT, *Ginga*, ASCA, and *Beppo*SAX also observed 4U 1820-30. Many spectral models have been applied to fit the observed X-ray spectra. For example, models which are a sum of a blackbody (BB) with thermal bremsstrahlung or a blackbody with a power law combined with exponential cutoff (CPL). A more detailed model were developed using a Comptonization spectrum by Sunyaev & Titarchuk (1980) (see CompST model in XSPEC) combined with a blackbody. Note, White et al. (1986) and Christian & Swank 1997) show that the models based on thermal bremsstrahlung mechanism are unphysical. The emission measures found using this model have to be of order $\sim 10^{60}$ cm^{-3} and they are too large for the plasma cloud near NS which radius is only of order of 10^6 cm.

Therefore the CPL and CompST components combined with a blackbody were applied to fit X-ray spectra of 4U 1820-30 [see e.g. Bloser et al. (2000)]. The BB temperature kT_{BB}, the photon index Γ and exponential cutoff energy E_C are the CPL+BB model parameters. Bloser et al. (2000) also included photoelectric absorption at low energies using the cross section of Morrison & McCamman (1983). White et al. 1986 and Hirano et al. (1987) show that a *Gaussian* at ∼6.7 keV is often needed to take into account a blend of K_α iron lines. Parsignault & Grindlay (1978) applying a power-law fit to the 4U 1820-30 ANS data (ANS

is an abbreviation of the Astronomische Nederlandse Satelliet) found X-ray spectral changes due intensity variations. They obtain that the photon index Γ changes from 2 at high count rates to 1.4 when count rate is low. In other words, they find that spectrum becomes harder when luminosity decreases. Stella, White, & Priedhorsky (1987) used the CPL+BB model to fit the data of the EXOSAT ME instrument in the energy range from 1 to 30 keV. These particular EXOSAT data were obtained during 1984 – 1985. The source was found at a *high* luminosity state (6.0×10^{37} erg s^{-1}) and a *low* luminosity state (2.0×10^{37} erg s^{-1}). The best-fit parameters of these EXOSAT spectra Γ, E_C and kT_{BB} are at 1.7, 12 keV and 2 keV respectively in the high state while Γ $\sim$2.5, E_C >30 keV, and kT_{BB}=2.3 keV in the low state.

Smale et al. (1994) analyzed the ASCA/GIS data for 4U 1820-30 which was observed in the low state in 1993. They fit the 0.6-11 keV spectrum using the CompST + BB model. The best-fit CompST parameters were around 3.6, 13.5 and 0.76 keV for the plasma temperature, optical and a blackbody temperature respectively. Christian & Swank (1997) reported on the *Einstein* (SSS + MPC) 1978 observation in the 0.5 – 20 keV energy range. They found the source was in the high state characterized by the luminosity of 5.5×10^{37} erg s^{-1} and the best-fit parameters of the CompST+BB model were very similar to those obtained using the ASCA data.

Piraino et al. (1999) and Kaaret et al. (1999) analyzed the first observations of 4U 1820-30 extended above $\sim$30 keV. For this analysis they used the observations implemented by the NFIs (0.1 – 200 keV) of *Beppo*SAX in 1998. The best-fit of the observed spectrum in the 0.3 – 40 keV energy range give kT_{BB}=0.47 keV, Γ=0.55, and E_C=4.5 keV for the CPL+BB model , whereas the best-fit parameters of the CompST+BB model are kT_{BB}=0.46 – 0.66 keV, kT_e=2.83 keV and τ=13.7. It is worth noting that the instruments with a response below 1 keV provide low values of kT_{BB}. Although, the range of luminosities and the best-fit parameters inferred using *Beppo*SAX and the CompST + BB model gave very similar values with respect to that obtained using the other instruments (see above).

The *Beppo*SAX Phoswich Detection System (PDS) could not detect the emission from 4U 1820-30 above 40 keV. Note, BATSE [see Bloser et al. 1996] also failed to find this source in the 20 – 100 keV range during the first four years of the CGRO. For the first time a high energy tail above 50 keV has been found by INTEGRAL in the hard state of 4U 1820-30 (Tarana et al. 2006), which put this source in the list of X-ray bursters which exhibit high-energy emission.

It is interesting to note that also other *atolls* can be described by similar spectral models. Lin et al. (2007), hereafter LRH07, pointed out that at the low-L_X end of the soft-state track a weak Comptonization component is needed. LRH07 modified the BPL and COMPTT

models applying their modifications to atolls Aql X-1 and 4U 1608-52. They were interested to find out how much energy is directly visible as a pure thermal radiation and thus one can obtain the remaining fraction for the Comptonized radiation f. In this sense this approach is similar to that using the COMPTB model (see below §3) . In this way, to account for specific spectra LRH07 describe the hard state by a BB+BPL model and the soft state by means of a three component model, MCD+BB+CBPL, where CBPL is a broken power law with the high energy cutoff taking into account the Comptonization effect.

In this Paper we show a thorough X-ray spectral-timing analysis of the data for 4U 1820-30 using the *Beppo*SAX and *RXTE*/PCA/HEXTE available observations which were made during 1998 – 1999 and 1996 - 2009 years respectively. Unlike the past spectral analysis, we adopt an unified model, capable describing the spectra observed during both the soft and hard states. The full list of observations used in our data analysis is present in §2 and Tables 1 and 2 while we describe, in detail our spectral model and spectral analysis using this model in §3. We interpret X-ray spectral-timing evolution when the source undergoes the spectral state transition in §§4−6. We explain our results in detail and come to the final conclusions in §§7−8.

2. Data Selection

We obtain broad band energy spectra of the source using data from three *Beppo*SAX Narrow Field Instruments (NFIs), namely the Low Energy Concentrator Spectrometer (LECS) with the 0.3−4 keV energy band, the Medium Energy Concentrator Spectrometer (MECS) with the 1.8−10 keV band and the Phoswich Detection System (PDS) with the 15-200 keV band [see Parmar et al. (1997); Boella et al. (1997); Frontera et al. (1997) respectively].

We use the SAXDAS data analysis package for data processing. We renormalized the LECS data based on the MECS data. We treat relative normalizations of the NFIs as free parameters when we proceed with model fitting, but we fix the MECS normalization at 1. Each of these normalizations is controlled if they are in a standard range for a given instrument[1]. Furthermore, we rebinned the spectra to obtain significant data points. The LECS spectra are rebinned using a binning factor which varies with energy (Sect. 3.1.6 of Cookbook for the BeppoSAX NFI spectral analysis) implementing rebinning template files in GRPPHA of XSPEC [2]. The PDS spectra are rebinned with a linear binning factor 2,

[1]http://heasarc.nasa.gov/docs/sax/abc/saxabc/saxabc.html

[2]http://heasarc.gsfc.nasa.gov/FTP/sax/cal/responses/grouping

namely we group two bins together leading to the bin width of 1 keV. For all of these spectra we use a systematic error of 1%. The *Beppo*SAX observations implemented in our analysis are shown in Table 1.

We also use publicly available the *RXTE* data sets (Bradt et al. 1993) which were obtained from April 1997 to March 2009. In total, they include 92 observations taken at different states of the source. The LHEASOFT/FTOOLS 5.3 software package were applied to process the data. Also for our spectral analysis we apply PCA *Standard 2* mode data, collected in the 3 – 20 keV energy range and the most recent release of PCA response calibration (ftool pcarmf v11.1). We use the standard dead time correction to the data.

A background corrected in off-source observations is subtracted from the data. We use only data from 20 to 150 keV energy in order to avoid the problems related to the HEXTE response and background determination. We apply the GSFC public archive to analyze all available data sets (see http://heasarc.gsfc.nasa.gov). We present a full list of observations covering the source evolution during different spectral state events in Table 2.

We implement an analysis of *thirteen* years *RXTE* observations of 4U 1820-30 for 7 intervals (see blue rectangles in Figure 1 in Titarchuk, Seifina & Frontera (2013), hereafter TSF13). We fitted the *RXTE* energy spectra using XSPEC astrophysical fitting software. For our data analysis we have also applied the public available 4U 1820-30 data in the energy range from 2 to 10 keV from the All-Sky Monitor (ASM/*RXTE*) for all observation scans.

According to ASM monitoring system 4U 1820-30 shows long-term variations with possible period $\sim$176 days of the 2 – 10 keV flux [see Fig. 1 in TSF13 and Priedhorsky & Terrell (1984); Simon (2003) and Wen et al. (2006)]. The count rate changes in the interval of $5-35$ counts s^{-1} throughout each cycle (see in Fig. 1 in TSF13). Our *RXTE* spectral studies are directed to investigate: i) the continuum spectrum, in particular, the hard X-ray tail and its evolution during long-term flux variations, ii) the variation ($\gtrsim$10 sec) of the best-fit spectral parameters for short- and long-term phases, and iii) the dependence of the spectral index and the electron temperature on the total flux and accretion rate. Data from the PCA and HEXTE detectors as well as *Beppo*SAX detectors have been used to constrain spectral fits, while ASM data provided long-term intensity state monitoring. Results of our long-term study of 4U 1820-30 are present, in detail, in the next sections and compared with our previous results for 4U 1728-34 and GX 3+1.

We use the broadband energy spectra of *Beppo*SAX (Boella et al. 1997) and *RXTE* (Bradt, Rothschild, & Swank 1993) combined with the high-timing resolution of *RXTE* to study short and long term spectral and timing evolution of *atoll* sources.

3. Spectral Analysis

Unlike the past analyses of the source spectral data discussed in the Introduction, in our study we make use of an unified model for both soft and hard states. In this way we have an opportunity to compare X-ray spectra of 4U 1820-30 in all states.

In our spectral model, we use an assumption, that the accretion material passes through the accretion disk [for example, through the standard Shakura-Sunyaev disk (Shakura & Sunyaev 1973)] and the transition layer (TL) (Titarchuk et al. 1998) where soft photons coming from the disk and NS surface are Comptonized off hot plasma (see also Fig. 2 in ST12). The Earth observer can also observe directly some fraction of these disk and NS seed photons.

Thus, our input model is a sum of Comptonization component ($COMPTB$), which is the XSPEC Contributed model[3], [see Farinelli et al. (2008), hereafter F08] and soft *blackbody* and line (*Gaussian*) components. The parameters of the $COMPTB$ component are the seed photon temperature kT_s, the electron (plasma) temperature kT_e, the energy index α $(= \Gamma - 1)$ of the Comptonization spectrum, the illumination fraction of the Comptonized region (TL), f $[f = A/(1 + A)]$ and the normalization of the seed photons illuminating the Comptonized region, N_{COMPTB}. We include a *Gaussian* component in the model characterized by the parameters E_{line}, σ_{line} N_{line} which are a centroid line energy, the line width and the normalization correspondingly. We also include a *blackbody* component and the interstellar absorption in our model characterized by the parameters: the normalization N_{BB}, the color temperature T_{BB} and a column density N_H respectively.

We fix the index of the seed photon spectrum $\alpha = 2$ (or $\gamma = \alpha + 1 = 3$). Namely, we suggest that this seed photon spectrum is a blackbody-like. We neglect the bulk inflow effect with respect to the thermal Comptonization assuming that a bulk parameter $\delta = 0$. The parameter $\log(A)$ of the $COMPTB$ component is fixed at 2 because the best-fit $\log(A) \gg 1$. Then $f = A/(1 + A)$ as the illumination fraction parameter is approximately 1, for any $\log(A) \gg 1$. We use a value of $N_H = 3.00 \times 10^{21}$ cm^{-2} estimated by Bloser et al. (2000) for 4U 1820-30. We find satisfactory fits using our model for both *Beppo*SAX and *RXTE* observations of 4U 1820-30 for all available data sets.

[3]http://heasarc.gsfc.nasa.gov/docs/software/lheasoft/xanadu/xspec/models/comptb.html

3.1. *Beppo*SAX data analysis

Table 3 shows the data analysis results for the broad-band *Beppo*SAX spectra. On the *top* of Figure 1 we present an example of the *Beppo*SAX spectrum along with its best-fit using our model while in the *bottom* panel we demonstrate $\Delta\chi$ (reduced χ^2=1.11 for 364 d.o.f). The line emission is clearly centered around 6.7 keV. We find that the width of this line of 0.8 keV is quite large and it is much wider than the instrumental response which width is smaller than 0.02 keV [4]. This broad emission line at 6.7 keV can be a result of illumination of highly ionized iron by X-ray continuum. Piraino et al. (2000) suggest that this broad line originates either in an ionized innermost disk region or in a hot corona above the disk. A combination of two absorption edges related to ionized iron, instead of a Gaussian line, can also describe this part of the spectrum (D'Ai et al. 2006). The *Laor* relativistically smeared line or reflection models can be also used to describe this line feature (see Ng et al. 2010 and Egron et al. 2011 respectively). However, Seifina & Titarchuk (2011) demonstrate that the model, wabs∗(blackbody+COMPTB+Gaussian), which includes a a *Gaussian* iron line, can successfuly fit the data for extensive *RXTE* and *Beppo*SAX observations of 4U 1728-34.

We can interpret this broad iron line detected in 4U 1820-30 in terms of reprocessing emission by a disk. In addition, we fit a smeared absorption edge in the 7−8 keV range using the *smedge* XSPEC model (see Ebisawa et al. 1994). The edge energy is 7.7±0.5 keV for the $wabs*(Bbody+Comptb+Gaussian)*smedge$ model which indicates to the presence of ionized material in the emission region. The smearing width is fixed at 10 keV. We include this edge component in the fits for all BeppoSAX data (see Table 3).

We obtain that $\alpha = 1.03 \pm 0.04$ (or $\Gamma = \alpha + 1 = 2.03 \pm 0.04$) for all analyzed *Beppo*SAX data, the seed photon temperature kT_s of the $COMPTB$ component is low variable and its value is around 1.3 keV whereas kT_{BB} varies in the interval from 0.58 to 0.69 keV (see Tables 1, 3 for details).

3.2. *RXTE* data analysis

For all *RXTE* fits we fix the *blackbody* temperature kT_{BB} =0.7 keV which is an upper limit of that in our analysis of the *Beppo*SAX data (see Table 3), because *RXTE* detectors cannot give us reliable spectra below 3 keV. In Table 4 we show the best-fit parameters of the *RXTE* spectra using our model. It is important to point out that for *all RXTE observations* of 4U 1820-30 the photon index Γ only slightly changes around 2 ($\Gamma = 1.99 \pm 0.02$) while the

[4]See ftp://heasarc.gsfc.nasa.gov/sax/cal/responses/98_11

best-fit kT_e varies in the 2.5−21 keV range.

However the determination of the iron line profile using the *RXTE* data is a difficult problem caused by the low-energy resolution of PCA/*RXTE* detector. Moreover, the inclusion of a *smedge* compoment in the spectral model for *RXTE* data does not improve fit quality any more. Therefore we apply our spectral model to *RXTE* data using a simple *Gaussian* as the line component without *smedge* modeling. The line width σ_{line} does not vary much and it is always in the interval from 0.9 to 1.3 keV during all spectral transitions. Therefore we fix σ_{line} at 1.2 keV for all spectra during fitting procedure. The values of the best-fit seed photon temperatures, $kT_s = 1-1.3$ keV are consistent with that obtained using the *Beppo*SAX data (see Table 3).

In Figure 2 we show the representative examples of $E * F(E)$ spectral diagrams of 4U 1820-30 during soft (*left panel*) and hard (*right panel*) state events. The best-fit *RXTE* spectra (*top* panels) in the model $wabs * (Bbody + CompTB + Gaussian)$ with $\Delta\chi$ (*bottom* panels) for the high-luminosity (*banana*) state [40017-01-11-00 observation, χ^2_{red}=1.00 for 78 d.o.f, *left panel*] and for the low-luminosity (*island*) state [94090-01-04-00 observation, χ^2_{red}=1.10 for 78 d.o.f, *right panel*]. The model best-fit parameters are $\Gamma = 1.99 \pm 0.02$, $kT_e = 2.94 \pm 0.01$ keV and $E_{Gauss} = 6.53 \pm 0.06$ keV for the *soft* state; $\Gamma = 2.00 \pm 0.04$, $kT_e = 12.54 \pm 0.09$ keV and $E_{Gauss} = 6.35 \pm 0.04$ keV for the *hard* state (see Table 4 for details). Violet, blue, red lines correspond to the *Gauss*, *Blackbody* and *CompTB* components, respectively.

In Figure 3 to illustrate the spectral evolution 4U 1820-30 we show six representative EF_E spectral diagrams for different electron temperatures of a Compton cloud [kT_e =2.9 keV (*red*), 3 keV (*blue*), 4 keV (*green*), 6 keV (*violet*), 10 keV (*pink*) and 12 keV (*black*)] applying the $wabs * (Blackbody + COMPTB + Gaussian)$ model during $island - banana$ state transitions.

We show how the TL electron temperature kT_e anti-correlates with the normalization $N_{\rm COMPTB}$ (proportional to $\dot{M}$) in Figure 4. For a comparison we add the points for 4U 1728-34 and GX 3+1 [see Seifina & Titarchuk (2011) and Seifina & Titarchuk (2012) respectively]. The electron temperature kT_e decreases and reaches a saturation about 3 keV when mass accretion rate increases [see an explanation of this effect in Farinelli & Titarchuk (2011), hereafter FT11].

Our spectral model applied to the spectral data of *Beppo*SAX and *RXTE* shows a robust performance throughout all data sets. Namely, a value of reduced $\chi^2_{red} = \chi^2/N_{d.o.f}$, where $N_{d.o.f}$ is a number of degree of freedom, is around 1.0 for most of observations. χ^2_{red} is about 1.5 for less than 3% of spectra with high counting statistics but χ^2_{red} is never above a rejection

limit of 1.6. Note the high residuals of the poor fit spectra (2 among 234 spectra for which χ^2=1.55) occur in the iron line region. As was shown by *Beppo*SAX analysis a shape of the iron line is more complex than a simple Gaussian (see discussion in §3.1). Probably, the fits of this line indicate to a broad line, which shape and width can be a result of scattering of the line photons in the hot plasma (TL) along with iron *smedge* effect there. However, we cannot resolve this line complexity using the *RXTE* data.

Thus using broad band *Beppo*SAX observations we can obtain the best-fit parameters of our spectral model whereas due to large-time coverage of 4U 1820-30 by *RXTE* we are capable to study the source spectral transitions in the 3−200 keV energy range.

4. Overall pattern of X-ray properties

4.1. Hardness-intensity diagram

To study the properties of 4U 1820-30 during the spectral transitions when the luminosity changes we use hard color (10-50 keV/3-50 keV) (HC) versus the 3-60 keV flux measured in units of 10^{-9} erg s^{-1} cm^{-2} [hardeness-intensity diagram (HID)].

In Figure 6 in TSF13 we demonstrate flux ratio HC versus the 3-60 keV flux using the *RXTE* data. As it appears from this Figure, 4U 1820-30 shows a "J" like diagonal shape in this diagram with upper *short* and lower *elongated* branches, which are joined at the lowest flux point. The spectral branches are indicated for the *island* state (IS), the *lower banana* state (LB) and the *upper banana* (UB) state. The direction of IS→LB→UB transition is shown by an arrow. The electron temperature kT_e changes from 21 keV to about 3 keV along the arrow line direction (compare with Fig. 4).

The identification of hardness-intensity diagram (HID) states are made using simultaneous timing and spectral analysis, and we have revisited the previous similar *RXTE* data analysis made by Bloser et al. (2000) and Migliari et al. (2004).

In particular, the hard color (HC) drops from 0.25 to 0.1 while the 3-60 keV flux is quasi constant when the source propagates from IS towards the LB. On the other hand HC rises from 0.12 to 0.35 with a simultaneous growth of the 3-60 keV flux when the source goes further from LB towards UB.

5. Evolution of X-ray spectral properties during spectral state transitions

A number of X-ray spectral transitions of 4U 1820-30 with luminosity variations have been detected by *RXTE* during 1996 – 2009 ($R1$ – $R7$ sets). We investigate common spectral−timing signatures which can be found for these spectral transition events. The source reveals different behaviors during *high-luminosity* and *low-luminosity* events.

5.1. Evolution of X-ray spectral properties during high-luminosity events

In Figures 5−6 we show the results of our spectral analysis of the *RXTE* observations applying the $wabs * (blackbody + COMPTB + Gaussian)$ model. On the top panels we present the *RXTE*/ASM count rate and the model fluxes from 3 to 10 keV and from 10 to 50 keV (see *blue* and *crimson* points respectively). The TL electron temperature kT_e as a function of time is shown in third panel from above. The temperature kT_e changes in the 2.9−4 keV interval during the time period MJD 50490−MJD 50700 and only slightly varies around 3 keV during MJD 51200−MJD 51500 time interval. The $COMPTB$ normalization N_{COMPTB} and the normalization of low temperature *blackbody* component N_{BB} (*crimson and blue* points respectively) are presented in the next-to-bottom panel of Figs. 5-6. One can clearly see that the $COMPTB$ normalization N_{COMPTB} correlates with variations of the ASM count rate and the 3 – 10 keV model flux. On the other hand the blackbody normalization N_{BB} only slightly varies.

5.2. Evolution of X-ray spectral properties during the low-luminosity events

Since the late April of 2009, 4U 1820-30 showed a prominent X-ray low-hard state at energies less than 10 keV as it was observed by the X-ray monitors on *RXTE* and $Swift$. We display the characteristics of the low-hard state obtained using the *RXTE* data in Figure. 7. Since 24 April 2009 (MJD 54945), the source was steadily brightening in the 15 – 50 keV band of the Swift/Burst Alert Telescope (BAT), with a daily average 0.032±0.002 cts/cm^2/s (145 mCrab) (Krimm et al. 2009). In contrast, the highest count rate detected by the $Swift$/BAT was 0.14 cts/cm^2/s.

The ASM/*RXTE* and PCA/*RXTE* light curves showed that 4U 1820-30 were in an extended low state from MJD 54944 to MJD 54982. The ASM count rate took a sharp drop at MJD 54944 while the flux began rising in the BAT monitor. The ASM count rate was very low, approximately 6.0±0.5 cts/s during this low state period, with respect to an usual average count rate of ∼20 cts/s. During the same time period the *RXTE*/PCA count rate

decreases from ∼4000 cts/s to ∼1000 cts/s. This kind of the long-time low state was not observed from 4U 1820-30 over the 10 – 15 year period. The typical low state duration varies from 1 to 2 weeks.

We also establish that the X-ray spectra of this source over the *low* luminosity state (MJD 54955 – 54982) are quite stable in terms of the *CompTB* normalization value. But the electron temperature kT_e of the *Comptonised* plasma increases from 3 keV up to 20 keV during MJD 54950 – 54960 period and after that kT_e gradually decreases again to 3 keV when the luminosity rises at the end of the quasi-plateau (at MJD 55000). In Table 4 we report the best-fit parameter values. During the IS-B transition period we find that the photon index Γ (or the spectral index $\alpha = \Gamma - 1$) is almost constant, i.e. only slightly varies around 2 (see the combined Figure 10 in TSF13).

5.3. Spectral state transitions in 4U 1820-30

In 4U 1820-30 the hard-soft state transition is observed as kT_e decreases from 15 – 20 keV to 3 keV (see Fig. 7). The outburst hard-to-soft state transitions are seen when a supply of the soft photons flux N_{COMPTB} dramatically increases (see Fig. 4 and Fig. 6 in TSF13). In general, following FT11, we consider the spectral state transitions in terms of the kT_e change. Thus the hard state is seen when the electron temperature reaches maximum, kT_e^{max}, whereas the soft state is observed when the electron temperature, T_e^{min} reaches minimum. Note that kT_e is well determined by the high energy cut-off of the spectrum, E_{cut} and can be well established by the spectral fits to the data. This spectral state definition is based on kT_e (or $E_{cut} \sim 2kT_e$). Unlike what occurs in the case of NS binaries, for a black hole case one can relate a spectral state change to the spectral (photon) index change [see Shaposhnikov & Titarchuk (2009), hereafter ST09].

We test the hypothesis of $\Gamma_{appr} \approx 2$ using χ^2-statistic criterion. We calculate the distribution of $\chi^2_{red}(\Gamma_{appr}) = \frac{1}{N}\sum_{i=1}^{N}\left(\frac{\Gamma_i - \Gamma_{appr}}{\Delta\Gamma_i}\right)^2$ versus of Γ_{appr}. and we find a sharp minimum of function $\chi^2_{red}(\Gamma_{appr})$ at 1 when $\Gamma_{appr} = 1.99 \pm 0.01$ and $\Gamma_{appr} = 1.99 \pm 0.02$ with confidence levels of 67% and 99% for 234 d.o.f. respectively (see the related Figure of $\chi^2_{red}(\Gamma_{appr})$ for 4U 1728-34 in ST11). The index Γ is almost constant when kT_e (see Fig. 8) and the $COMPTB$ normalization, L_{39}^{soft}/d_{10}^2 changes (see below). FT11 based on the analysis of *Beppo*SAX data propose that Γ is about 2 for quite a few NS sources. FT11 also define the spectral state using a value kT_e and they demonstrate that $\Gamma = 2 \pm 0.2$ (or $\alpha = 1 \pm 0.2$) when kT_e varies in the 2.9−21 keV interval.

It should be noted that not all NSs shows spectral state transitions but quite a few NSs

exhibit them. For instance, so called atoll-sources (such as 4U 1820-30), usually demonstrate IS – B transitions. Particularly during such transitions, it can be possible to differ NS from BH. Specifically, NSs and BHs show drastically different variations of spectral characteristics. NSs, as examples of 4U 1820-30 and 4U 1728-34, indicate to variabilities of kT_e and mass accretion rate $\dot{M}$ along with a quasi-constant index Γ about 2. Meanwhile, BHs demonstrate a monotonic growth of Γ when $\dot{M}$ increases and succeeded by its final flattening (saturation) [see ST09].

6. Spectral−timing correlations during spectral state transitions

We analyze the *RXTE* light curves applying the *powspec* task taken from FTOOLS 5.1. We implement the timing analysis *RXTE*/PCA data which we perform in the 13-30 keV range applying the *event* mode with time resolution of 1.2×10^{-4} s. We make power density spectra (PDS) in 0.1−500 Hz frequency range with 0.001−second time resolution. The Poissonian statistics contribution was subtracted. We apply QDP/PLT package[5] for PDS modeling.

6.1. Spectral and timing properties during low luminosity state transition

In Figure 12 in TSF13 we present a generic behavior of X-ray timing−spectral characteristics for the *low* luminosity state at *R*7 (2009) transition events. We plot PDSs (*left* column) along with the $EF(E)-$ spectral diagram (*right* column) for six moments at MJD = 54947.6/54956.5, 54958.6/55002.6 and 54997.7/54960.36, covering different transition phases. At the *bottom* we demonstrate PDSs for the 15−30 keV energy range (*left* column) and plot along with the $E*F(E)-$spectral diagram (*right* column) for A−C time events (see upper panel). All points [(events) A *red* (ID 94090-01-01-00), A *blue* (ID 94090-01-02-03), B *red* (ID 94090-01-02-02), C *red* (ID 94090-01-04-03)], except B (*blue*) and C (*red*), are related to IS (broadband noise, no VLFN).

PDSs denoted by B (*blue*, ID 94090-02-02-00) and C (*red*, ID 94090-0103-00) exhibit the *island−lower banana* state transition. For the *blue* PDS the VLFN (very low frequency noise) appears as a band-limited noise component which transforms into QPO (broad Lorentzian with ν_h centroid frequency at 7 – 10 Hz). We present power density spectra (PDSs) (panels A1, B1, C1) along with the corresponding $E*F(E)-$spectral diagrams (panels A2, B2, C2).

[5]http://heasarc.gsfc.nasa.gov/ftools/others/qdp/qdp.html

The related PDSs and energy spectral data are shown by blue and red points respectively. On the left panel we also show the electron temperature kT_e associated with a given PDS.

6.2. Spectral and timing properties during high luminosity state transition

To compare with Figure 12 in TSF13, we show an evolution of spectral−timing characteristics during the *high* luminosity state in Figure. 9. Here on the *top* panel we display the ASM light curve during *high* luminosity interval at $R3$ (1999) transition events. Red/blue points A, B, and C are related to the moments at MJD = 51283.6/51300, 51313.7/51330.5 and 51389.4/51396.26, covering different transition phases. On the *bottom left* and *right* panels we present PDSs for 15-30 keV energy range and the $E*F(E)$−spectral diagram correspondingly, for A (*red*, top), B (*blue*, middle) and C (*blue*, bottom) points of X-ray light curve (see the upper panel). All points are related to the *banana* state with relatively strong broadband noise and VLFN with QPOs which is at $\nu_l \sim 6$ – 7 Hz for C moment (*red*). The PDSs in panel C (*blue*) and (*red*) illustrate the *island−lower banana* state transition. Here the VLFN appears, band-limited noise component transforms into QPO [a broad Lorentzian with ν_h centroid frequency at 7−10 Hz, C *red* (40017-01-12-00)]. The power spectra (panels A1, B1, C1) correspond to $E*F(E)$ diagrams (panels A2, B2, C2). The corresponding energy spectra of 4U 1820-30 are related to the electron temperature of 3 keV.

In Figure 10 we illustrate a typical power spectrum of 4U 1820-30 for different X-ray spectral states (shown on the right panel). The electron temperature values of corresponding energy spectra are indicated at the right vertical axis. The power spectra in the extreme island state (EIS), island state (IS, multiplied by factor 10^{-2} for clarity), lower left banana state (LLB, $\times 10^{-4}$), lower banana state (LB, $\times 10^{-6}$) and upper banana state (UB, $\times 10^{-8}$) are presented from the top to the *bottom*. The histograms show the best fits to the power spectra, which consist of three components: VLFN the peaked noise component, low-frequency QPOs (ν_l and ν_h) and high frequency feature ν_{hHz} (see van Straaten, van der Klis & Mendes 2003 for details of terminology).

6.3. Comparison of spectral and timing characteristics of *atoll* sources 4U 1820-30, GX 3+1 and 4U 1728-34

In this Paper, we also study the correlations of X-ray spectral−timing characteristics and $\dot{M}$ in a number of *atolls* during their spectral transitions searching for similarities and differences between *atoll* sources. In this way we can present a comparative analysis for

three *atoll* sources: 4U 1820-30, GX 3+1 and 4U 1728-34 applying the same spectral model which consists of low temperature *Blackbody*, *Comptonized* continuum and *Gaussian* line component.

6.3.1. Constancy of the photon index

We demonstrate that *atolls* 4U 1820-30, GX 3+1, 4U 1728-34 show a similar pattern of the photon index Γ vs $\dot{M}$ (or N_{COMPTB}). Namely, the photon index Γ only slightly varies around 2 (see Fig. 11). Following to FT11, ST11 and ST12, we can suggest that the cooling flow of soft disk photons is much less less than the energy release in the transition layer (TL) for each of these three sources.

6.3.2. The difference and similarity of kT_e ranges in 4U 1820-30, GX 3+1 and 4U 1728-34

One can see from Figure 12, that the ranges of kT_e for an individual state evolution of these three sources are different. The electron temperature kT_e changes in 4U 1728-34 from 3 to 15 keV whereas kT_e varies within much narrow range of kT_e around 3 keV in GX 3+1. In turn, source 4U 1820-30 demonstrates a wider interval of kT_e in which kT_e varies from 2.9 keV to 21 keV similar to some extent to the temperature change in 4U 1728-34. Note, that in a low temperature regime 4U 1820-30 and GX 3+1 are similar in terms of normalization $N_{\rm comptb}$ =(4 – 15)$\times L_{39}/D_{10}^2$, or mass accretion rate, (see Fig. 4) and Comptonized fraction f = 0.2 – 0.8 (see Fig. 12). While 4U 1820-30 and 4U 1728-34 are similar for a range of the normalization $N_{\rm comptb}$ =(2 – 4)$\times L_{39}/D_{10}^2$ (see Fig.4) and $f = 0.5 - 0.8$ (see Fig. 12) for high temperature regime. However, in contrast to 4U 1728-34, the source 4U 1820-30 has an additional branch of intermediate temperatures (8 – 12 keV) when the Comptonized fraction is relatively low, $f < 0.5$ (see Fig. 12). Note that all objects have a common temperature interval 3 – 4 keV when $N_{\rm comptb}$ (or mass accretion rate) is relatively high.

Thus according to FT11, ST11, ST12 and the present study, the electron temperature kT_e for *atolls* and $Z-$sources varies in the 2.5$-$25 keV range. Specifically, the change of kT_e around 3 keV is similar for all three source 4U 1820-30, GX 3+1 and 4U 1728-34. The minimum value of kT_e at 2.5 keV occurs at the peak luminosity for 4U 1728-34 (see ST11), during a local rise of luminosity for GX 3+1 (ST12) and at high luminosity phases for 4U 1820-30.

For all of these three objects, the values of color seed photon temperatures $kT_s = 1.1-1.7$

keV and blackbody temperatures $kT_{BB} \simeq$0.6 keV are comparable (see Table 5). Contrary, the variability extent of kT_e is not similar. The reason for that difference of electron temperature ranges is evident. Sources 4U 1820-30 and 4U 1728-34 show a complete cycle of state evolution: *island−lower banana* (LB)- *upper banana* (UB) stages for 4U 1820-30 and for 4U 1728-34 it is *extreme island* state (EIS)−*upper banana* (UB) state (see Di Salvo et al. 2001; ST11). But GX 3+1 demonstrates a short evolution behavior on the CCD from LB to UB. This evolution picture is also clear from Figure 12 which shows that the track of GX 3+1 is only a part of the full track [see definition of a state sequence and the standard *atoll-Z* scheme in Hasinger & van der Klis (1989)].

Note, that 4U 1820-30 shows almost the same kT_e range as that in 4U 1728-34 and almost similar timing evolution. But clear differences between these *atolls* one can see from Figure 17 in TSF13 where we show spectral hardness (10 – 50 keV/3 – 50 keV) vs flux in 3 – 60 keV range. In fact, 4U 1728-34 (*blue* points) is fainter and harder and demonstrates much wider spectral hardness range than that in 4U 1820-30 (*red* points).

6.3.3. Comparison of spectral evolution as a function of the luminosity for 4U 1820-30, GX 3+1 and 4U 1728-34

Now we present a comparison of X-ray spectrum evolution for sources 4U 1820-30, GX 3+1 and 4U 1728-34 based on *luminosity* value which is presumably proportional to *Comptb* normalization and, consequently, to mass accretion rate taking into account that their distances to the Earth are similar (see Table 5). For 4U 1820-30 the distance range is within of 5.8 – 8 kpc (Shaposhnikov & Titarchuk, 2004), whereas for 4U 1728-34 and GX 3+1 the distances are estimated as 4.5 kpc and 4.2−6.4 kpc respectively [see van Paradijs (1978) and Kuulkers & van der Klis (2000)].

We show the $CompTB$ normalization (related to the soft photon *luminosity* value) for these sources as a function of kT_e in Figure 4. 4U 1820-30 subtends a wider interval in $CompTB$ normalization than that for 4U 1728-34. Note, that in the high luminosity state (or $N_{\rm comptb}$) 4U 1820-30 is similar to GX 3+1: $N_{\rm comptb} = (4 – 15)\times L_{39}/D_{10}^2$, Comptonized fraction f =0.2 – 0.8 (see Fig. 12) and the electron temperatures kT_e are low variable around 3 keV. While in the low luminosity state 4U 1820-30 is closer to source 4U 1728-34: $N_{\rm comptb} = (2 – 5)\times L_{39}/D_{10}^2$ (see Fig.4), f =0.5 – 0.8 and kT_e changes from 5 to 20 keV (see Fig. 12).

6.3.4. The difference and similarity of time scales of state evolution for 4U 1820-30, GX 3+1 and 4U 1728-34

We should point out that all these three *atoll* source show the transitions between low luminosity and high luminosity states over different time scales. Specifically, the time scales of X-ray flux variability for 4U 1728-34, 4U 1820-30 and GX 3+1 probably dictated by variability of mass accretion rate, are ∼10 d, 100 d and 1000 d, respectively. However, these sources demonstrate LB – UB transition and make it in the narrow interval of low temperature kT_e (around 3 keV) and during the same short time interval (hours – day). We remind the reader that the comparison between these three sources is facilitated by the fact that they show almost the same kT_{BB} and kT_s temperature values and they are located at approximately the same distance. The only difference of spectral evolution of these objects is related to different ranges of the electron temperature of the Comptonized component.

6.3.5. Correlation of illumination parameter f versus electron temperature kT_e and its relation with different stages in the color-color diagram

Using Table 5 one can see that the ranges of the best-fit illumination fraction f are $0.2 - 1.0$, $0.2 - 0.9$ and $0.5 - 1$ for 4U 1820-30, GX 3+1 and 4U 1728-34 correspondingly. These values of f indicate to different geometry of the transition layer (TL) and thus to different illumination for these X-ray sources.

In Figure 12 we demonstrate that the electron temperature kT_e directly correlates with a sequence of CCD states, EIS-IS-LLB-LB-UB [see Hasinger & van der Klis (1989) for this CCD classification]. Note that ST12 reveal a relation between spectral states, kT_e and f for *atoll* sources GX 3+1 and 4U 1728-34. We show these $kT_e - f$ relations for these two atolls in Figure 12. The direction in which the inferred $\dot{M}$ increases is indicated by arrows.

Now we present three different tracks on the $kT_e - f$ diagram for three source 4U 1820-30, GX 3+1 and 4U 1728-34 and show how these tracks are related to the standard CCD sequence (see Fig. 12). The track of 4U 1820-30 consists of three segments (branches) related to kT_e: high (12 – 21 keV), intermediate (7 – 12 keV) and low temperature (2.9 – 6 keV) ones, wherein each segment has a negative correlation of kT_e and f. In turn, GX 3+1 demonstrates the only, so called, *low temperature* branch track. Namely, when the fraction f increases, kT_e decreases from $\sim$ 4.5 keV to $\sim$ 2.3 keV. While for 4U 1728-34 we see a more complicated pattern, but in contrast to 4U 1820-30 and GX 3+1, has a segment with positive correlation of kT_e vs f from 4 to 12 keV. Specifically, at the high temperature state (EIS), f only slightly changes from 0.9 to 1 when kT_e decreases. As kT_e further drops from

12 keV to 4 keV, f also drops from 0.9 to 0.5. Finally, f goes up from 0.5 to 0.8 when the source enters to the low-temperature state (LB-UB). As a result, we demonstrate that the CCD state evolution can be also seen using the $kT_e - f$ correlation.

6.4. Comparison of spectral hardness diagrams for atolls 4U 1820-30, GX 3+1 and 4U 1728-34

We use the plot HC (10-50 keV/3-50 keV) versus the 3 – 60 keV flux in form of HIDs for three sources: 4U 1820-30 (*red*), GX 3+1 (*green*) and 4U 1728-34 (*blue*) (see Fig. 17 in TSF13) to compare transition properties of these *atolls* in terms of their flux (or luminosity). In fact, 4U 1820-30 shows a "J" like inclined (or diagonal) shape in HID with upper *short* and lower *elongated* branches (see Fig. 6 in TSF13). The *short* branch is close to the low luminosity state, whereas the *elongated* branch covers the wide luminosity range.

Our comparative analysis of HID track branches for 4U 1820-30, GX 3+1 and 4U 1728-34 indicates to similar physical properties of these objects. The spectral and timing characteristics are very similar along corresponding segments. Specifically, the *short* branch of a "J" like track of 4U 1820-30 is adjacent to low luminosity area of 4U 1728-34 (*blue* points) and it is related to a high electron temperature regime of 4U 1820-30, as in 4U 1728-34. In turn, the *elongated* branch of 4U 1820-30 is closer to GX 3+1 (*green* points) branch area and it is associated with low electron temperatures kT_e (3 – 4 keV) and softer spectra, which are also seen in GX 3+1.

Note that among considered *atolls* superbursts are only observed in GX 3+1 and 4U 1820-30 during *elongated* branch. Furthermore, superbursts are detected at low−soft states, i.e. during low luminosity interval of light curve when electron temperature kT_e is about 4 keV. Thus 4U 1820-30 shows a property similar to GX 3+1 and it is situated at an *intermediate position* between 4U 1728-34 and GX 3+1 in terms its luminosity. This observational fact can be related to the same *intermediate* rate of mass transfer in these two sources, 4U 1820-30 and GX 3+1 [see also a review by van der Klis (1994)]. The comparison of HIDs allows to diagnose physical properties of different objects with adjacent HID tracks.

7. Discussion

7.1. Stability of photon index is a signature of NS source

Thus we demonstrate that the photon spectral index only slightly varies around 2 using numerous observations of NS sources 4U 1820-30, GX 3+1 (ST12) and 4U 1728-34 (ST11) by *Beppo*SAX and *RXTE*. In Figures 8, 11 and 13 ($left$ column) we show Γ as a function of the spectral model parameters: kT_e (in keV), $N_{COMPTB}-$normalization, and illumination fraction f. These results for NS 4U 1820-30 have been obtained when we apply our thermal Comptonization model to *Beppo*SAX and extensive *RXTE* observations. FT11 and ST11 also investigate and find the photon (energy) index stability in other observations of NS binaries. We explain this index stability using the Comptonization model. Namely, the photon (energy) index is almost constant when the soft photon flux illuminated the transition layer (TL) is much less than the gravitational energy release in TL (see e.g. ST12). This model of the index stability can probably resolve the index stability effect now clearly established in these three NS sources using extensive *Beppo*SAX and *RXTE* observations.

7.2. On the *hard tail* origin in *atoll* source 4U 1820-30

The radio emission detected from 4U 1820–30 (Migliari et al. 2004) suggests the presence of a jet, which may also generate an extended power-law X-ray emmision. In this case, the power law can be a result of the inverse Compton effect on nonthermal electrons of the jet. Note, X-ray nonthermal power-law tails are also observed in soft states of BHs see for example a review by ST09; see also McConnell et al. (2002) and Wardzi'nski et al. (2002) on the detection of the extended hard tails in the hard states of BHs, Cyg X-1 and GX 339-4 respectively, and NS Z-sources [see Di Salvo et al. (2000); Farinelli et al. (2005); D'Amico et al. (2001); Asai et al. (1994)]. However these extended hard tails are also found in *atolls* [see e.g. Piraino et al (1999)].

Additive models that have been applied to fit the spectra of 4U 1820-30, need to use an additional power-law component (pure one or as a component of CompPS) to describe a hard spectral tail above 80 keV [see e.g. Tarana et al. (2006)]. However such an approach invokes an unknown non-thermal origin of *hard tail* emission. On the other hand our suggestion allows us to explain X-ray spectra of 4U1820-30 in *all spectral states* using the same model without a specific composition of the model components at different states. In fact, in our model (see §5.2 and §6.1) we describe the *hard tail* emission using the thermal Comptonization component in which the TL electron temperature kT_e increases up to 20 keV and the illumination factor f decreases as the source goes to the hard state (see Figs.

3, 12).

8. Conclusions

We analyze the X-ray spectral and timing characteristics of 4U 1820-30 observed during the hard-soft state transitions. We find a number of spectral transitions in 4U 1820-30 using *BeppoSAX* and *RXTE* data.

For our investigation we take an advantage the *Beppo*SAX broad spectral extension over the 0.3−200 keV range and abundant $RXTE$ observations taken in the 3−200 keV energy coverage.

We demonstrate that the X-ray broad-band spectra can be successfully fit by composition of the *Blackbody*, Comptonization (*Comptb*) and *Gaussian*−line components for *all spectral states*. Also we show an observable relation of the photon index Γ and the normalization of the Comptonized component, *Comptb* which is proportional to $\dot{M}$. We demonstrate the stability of the photon index $\Gamma \sim 2$ when the source goes from the hard state to soft state, in other words when the electron temperature of Comptonized region (TL), kT_e decreases from 21 to 3 keV (see Fig. 8).

We also show that Γ only slightly varies with the *Comptb* normalization ($\propto \dot{M}$). Note, this stability of the index in NS sources has been recently suggested for a number of other NSs, Sco X-1, Cyg X-2, GX 17+2, GX 3+1, GX 340+0, GX 349+2, X 1658-298, 1E 1724-3045, GS 1826-238, which were analyzed using *Beppo*SAX data (see details in FT11, ST11, ST12). The use of the disk *seed* photon normalization, (*Comptb*), which is proportional to $\dot{M}$, is fundamental in order to find the stability of Γ during the hard-soft state transition. We do find the stability (constancy) of the photon index of Comptonized component versus both the *Comptb* normalization and the electron temperature kT_e about 2 for all spectral states. In our analysis of NS sources (see FT11, ST11, ST12, Seifina et al. 2013 and this Paper) we do not find any particular case in which the photon index Γ changes beyond the limits 2 ± 0.1. Thus this index stability can be taken as an intrinsic property of neutron star (NS) binaries (*as a NS signature*), which is drastically different from that in black hole binaries [e.g., GX 339-4, GRO J1655-40, XTE J1650-500, XTE J1550-564, 4U 1543-47, XTE J1859+226, H 1743-322, (ST09), GRS 1915+105 (TS09), SS 433 (ST10)], where Γ monotonically rises during the hard−soft state transition and it follows by its saturation at high $\dot{M}$−values (see Fig. 13). In Figure 13 we show the $\Gamma - \dot{M}$ correlation for a number of BHs (*right* column) and that Γ is almost independent of $\dot{M}$ in NSs (*left* column). Indices Γ in BHs show clear correlation with $\dot{M}$, or with the normalization L_{39}/D_{10}^2 [where L_{39} is a

flux of soft (seed) photons]. The $\Gamma - \dot{M}$ correlation is followed by $\Gamma-$saturation when mass accretion rate $\dot{M}$ exceeds the Eddington limit. The behavior of Γ vs $\dot{M}$ for a considered sample of NSs (4U 1820-30, 4U 1728-34 and GX 3+1) is drastically different from that for given examples of BHs.

A relatively wide interval of the illumination fraction $f = 0.2 - 1$ which we obtain in the framework of our model, point to variable soft (disk) photon illumination of the transition layer in 4U 1820-30. Using *Beppo*SAX data we also find two types of blackbody photons. One type is characterized by color temperature of 0.7 keV, which is typical for the disk photons and another one is related to 1.3 keV, which can be associated with NS surface temperature.

We detect an evolution of 6 – 20 Hz QPOs and noise components during the *island – banana* state evolution (LLB-UB) (see Fig. 9).

Our observational results establishing the constancy of the photon index Γ *in 4U 1820-30 confirm the theoretical arguments of FT11 and ST11 that the TL energy release* Q_{cor} *dominates the soft photon flux illuminating the transition layer (TL) which comes from the accretion disk,* Q_{disk}*. We argue that the found stability of* Γ *is an intrinsic NS signature as in BH binaries* Γ *monotonically increases with* $\dot{M}$ *followed by its saturation at high values of* $\dot{M}$ *(see ST09).*

LT acknowledges discussion with Chris Shrader and his thorough editing of the manuscript and also we appreciate comments of the referee which substantially improve a quality of the presented material.

REFERENCES

Asai, K., Dotani, T., Mitsuda, K., Nagase, F., Kamado, Y., Kuulkers, E., & Breedon, L. M. 1994, PASJ, 46, 479

Bloser, P. F., Grindlay, J. E., Kaaret, P. et al. 2000, ApJ, 542, 1000

Bloser, P. F., et al. 1996, A&AS, 120, 275

Boella, G. et al. 1997, A&AS, 122, 327

Bradt, H.V., Rothschild, R.E. & Swank, J.H. 1993, A&AS, 97, 355

Clark, G.W., Li, F.K., Canizares, C., Haykava, S., Jernigan, G., Lewin, W.H.G., 1977, MNRAS, 179, 651

Cornelisse, R., et al. 2003, A&A, 405, 1033

Costantini, E. et al. 2012, A&A, 539, 32

Chou, Y. & Grindlay, J. E. 2001, ApJ, 563, 934

Christian, D. J., & Swank, J. H. 1997, ApJS, 109, 177

D' Ai, A. et al. 2006, A&A, 448, 817

D'Amico, F., Heindl, W. A., Rothschild, R. E., & Gruber, D. E. 2001, ApJL, 547, L147

Di Salvo, T., Iaria, R., Burderi, L., & Robba, N. R. 2000, ApJ, 542, 1034

Ebisawa, K., et al. 1994, PASJ, 46, 375

Egron, E., Di Salvo, T., Burderi, L., et al. 2011, A&A, 530, A99

Hirano, T., Hayakawa, S., Nagase, F., Masai, K., & Mitsuda, K. 1987, PASJ, 39, 619

Farinelli, R. & Titarchuk, L., 2011, A&A, 525, 102 (FT11)

Farinelli, R., Titarchuk, L., Paizis, A. & Frontera, F. 2008, ApJ, 680, 602, (F08)

Farinelli, R., Frontera, F., Zdziarski, A. A., Stella, L., Zhang, S. N., van der Klis, M., Masetti, N., & Amati L. 2005, A&A, 434, 25

Ford, E. C., van der Klis, M., Mendez, M., et al. 2000, ApJ, 537, 368

Frontera, F. et al. 1997, SPIE, 3114, 206

Geldzahler, B. J., 1983, ApJ, 264, L49

Gierli'nski, M., Zdziarski, A. A., Poutanen, J., Coppi, P. S., Ebisawa, K., & Johnson, W. N. 1999, MNRAS, 309, 496

Grindlay, J., Gursky, H., Schnopper, H., Parsignault, D. R., Heise, J., Brinkman, A. C., & Schrijver, J. 1976, ApJ, 205, L127

Grindlay, J.E. & Seaquist, E.R. 1986, ApJ, 310, 172

Hasinger, G. & van der Klis, M. 1989, A&A, 225, 79

Hirano, T. Haykawa, S., Nagase, F. Masai, K. & Mitsuda, K. 1987, PASJ, 39, 619

Kaaret, P., Piraino, S., Bloser, P. F., Ford, E. C., Grindlay, J. E., Santangelo, A., Smale, A. P., & Zhang, W. 1999, ApJ, 520, L37

Krimm, H. A. et al., 2009, ATel N 2071

Kuulkers, E., den Hartog, P. R., in't Zand, J. J. M., Verbunt, F. W. M., Harris, W. E., & Cocchi, M., 2003, A&A, 399, 663

Kuulkers, E. & van der Klis, M. 2000, A&A, 356, L45

Kuśmierek, K., Madej, J. & Kuulker, E. 2011, MNRAS, in press (arXiv: 1105.1525v)

Lewin, W.H.G., van Paradijs, J., & Taam, R.E. 1993, Space Sci. Rev., 62, 223

Lin, D., Remillard, R., & Homan, J. 2007, Apj, 667, 1073 (LRH07)

McConnell, M. L., et al. 2002, ApJ, 572, 984

Marti, J., Mirabel, I.F., Rodriguez, L.F., & Chaty, S. 1998, A&A, 332, L45

Migliari, S, Fender, R.P., Rupen, M. et al. 2004, MNRAS, 351, 186

Morrison, R. & McCammon, D. 1983, ApJ 270, 119

Ng, C., Daz, T. M., Cadolle, B. M., & Migliari, S. 2010, A&A, 522, A96

Oosterbroek, T., Barret, D., Gianazzi, M., & Ford, E. C. 2001, A&A, 366, 138

Parmar, A. N., et al. 1997, A&AS, 122, 309

Parsignault, D. R., & Grindlay, J. E. 1978, ApJ, 225, 970

Piraino, S., Santangelo, A., & Kaaret, P. 2000, A&A, 360, 35

Piraino, S., Santangelo, A., Ford, E. C., & Kaaret, P. 1999, A&A, 349, L77

Priedhorsky, W. & Terrell, J., 1984, ApJ, 284, L17

Rappaport, S., Nelson, L. A., Ma, C. P., & Joss, P. C. 1987, ApJ, 322, 842

Rich, R. M., Minniti, S., & Liebert, J. 1993, ApJ, 406, 489

Seifina, E. & Titarchuk, L. 2012, ApJ, 747, 99 (ST12)

Seifina, E., Titarchuk, L. & Frontera, F. 2013, ApJ, accepted

Seifina, E. & Titarchuk, L. 2011, ApJ, 737, 128 (ST11)

Seifina, E. & Titarchuk, L. 2010, ApJ, 722, 586 (ST10)

Sidoli, L., Parmar, A. N., Oosterbroek, T., Stella, L., Verbunt, F., Masetti, N., & Dal Fiume, D. 2001, A&A, 368, 451

Simon, V. 2003 , A&A, 405, 199

Shakura, N. I., & Sunyaev, R. A. 1973, A&A, 24, 337

Shaposhnikov, N., & Titarchuk, L. 2009, ApJ, 699, 453

Shaposhnikov, N., & Titarchuk, L. 2004, ApJ, 606, L57

Smale, A. P., Dotani, T., Mitsuda, K., & Zylstra, G. 1994, BAAS, 26, 872

Smale, A. P., Zhang, W., & White, N. E. 1997, ApJ, 483, L119

Stella, L., White, N. E., & Priedhorsky, W. 1987, ApJ, 315, L49

Strohmayer, T. & Bildsten, L., 2004, "New view of thermonuclear bursts", in Compact Stellar X-Ray Sources, Cambridge Astrophys. Ser. 26, eds. W.H.G. Lewin and M. van der Klis

Strohmayer, T. E. & Brown, E. F. 2002, ApJ, 566, 1045

Sunyaev, R. A. & Titarchuk, L. G. 1980, A&A, 86, 121

Tarana, A., Bassano, A., Ubertini, P. and Zdziarski, A. A. 2006, ApJ, 654, 494

Titarchuk, L., Lapidus, I.I. & Muslimov, A. 1998, ApJ, 499, 315

Titarchuk, L. Seifina, E. & Frontera, F. 2013, ApJ, 767, (TSF13)

Titarchuk, L. & Seifina, E. 2009, ApJ, 706, 1463

Vacca, W. D., Lewin, W. H. G. & Paradijs, J. 1986, MNRAS, 220, 339

van Paradijs, J. 1978, Nature, 274, 650

Wardzi'nski, G., Zdziarski, A. A., Gierli'nski, M., Eric Grove, J., Jahoda, K., & Neil Johnson, W. 2002, MNRAS, 337, 829

Wardzi'nski, G., Zdziarski, A. A., Gierli'nski, M., Grove, J.E., Jahoda, K., & Neil Johnson, W. 2002, MNRAS, 337, 829

Wen, L., Levine, A. M., Corbet, R. H. D., & Bradt, H. V. 2006, ApJS, 163, 372

Wijnands, R. & van der Klis, M., 1999, ApJ 514, 939

White, N. E., Peacock, A., Hasinger, G. et al. 1986, MNRAS 218, 129

Zdziarski, A. A., Wen, L., & Gierlinski, M. 2007, MNRAS, 377, 1006

Zhang, W., Smale, A. P., Strohmayer, T. E., & Swank, J. H. 1998, ApJ, 500, L171

Table 1. The list of *Beppo*SAX observations of 4U 1820-30 used in analysis.

Obs. ID	Start time (UT)	End time (UT)	MJD interval
20105004	1997 Oct. 2 06:45:23	1997 Oct. 2 19:09:36	50723.2-50723.8
20537004	1998 Apr. 17 04:31:23	1998 Apr. 18 02:55:28	50920.1-50921.1[1]
20537005	1998 Sept. 23 12:44:56	1998 Sept. 24 15:30:05	51079.5-51080.6[1]

Reference. (1) Kaaret et al. (1999)

Table 2. The list of groups of *RXTE* observations of 4U 1820-30

Number of set	Dates, MJD	RXTE Proposal ID	Dates UT	Ref.
R1	50204-50207	10074	May 1 – 4, 1996	1
	50151, 50235	10076	March 9, June 1, 1996	1
	50371-50386	10075	Oct. 15 – 30, 1996	1, 2, 3, 4
R2	50488-50701	20075	Feb. 9 – Sept. 10, 1997	1, 3, 4, 5, 6, 7
R3	50920-51467	30053, 30057	Apr. 4, 1998 – Oct. 16, 1999	3
	51206-51956	40017, 40019	Jan. 28, 1999 – June 4, 2003	
R4	51996-51999	60030	March 28 – 31, 2001	
	52355, 52429	40017	March 22, 2002; June 6, 2003	
	52439	70031	June 14, 2002 13:21:52 – 14:14:40	
	52482-52808	70030	July 23, 2002 – June 18, 2003	8
	52894	80105	Sept. 12, 2003 05:41:04 – 09:36:32	8
R5	53258-53591	90027	Sept. 10, 2004 – Aug. 9, 2005	
	53692-53693	91435	Nov. 18 – 19, 2005	
R6	53959-54028	91151	Aug. 12 and Oct. 9, 2006	
	53921-54306	92030	July 5, 2006 – July 25, 2007	
	54126-54129	70030	Jan. 26 – 29, 2007	
R7	54947-55002	94090	Apr. 26 – June 20, 2009	9
	54947-55116	92030	Sept. 8 – Oct. 12, 2009	

References: (1) Chou & Grindlay (2001); (2) Smale et al. (1997); (3) Kaaret et al. (1999); (4) Zhang et al. (1998); (5) Bloser et al. (2000); (6) Kuśmierek et al. 2011; (7) Shaposhnikov & Titarchuk (2004); (8) Migliari et al. (2004); (9) Krimm et al. (2009)

Table 3. Best-fit parameters of spectral analysis of *Beppo*SAX observations of 4U 1820-30 in 0.3-200 keV energy range[†]. Parameter errors correspond to 90% confidence level.

Observational ID	MJD, day	T_{BB}, keV	$N_{BB}^{\dagger\dagger}$	T_s, keV	$\alpha = \Gamma - 1$	T_e, keV	log(A)	N$_{COMPTB}$	E$_{line}$, keV	$N_{line}^{\dagger\dagger}$	χ^2_{red} (d.o.f.)
20105004	50723.28	0.63(3)	2.33(2)	1.35(2)	1.00(4)	3.25(2)	-0.11(5)	3.45(2)	6.7(1)	0.45(2)	1.11(364)
20537004	50920.19	0.58(1)	2.74(3)	1.24(5)	1.01(5)	3.42(2)	-0.10(6)	4.42(6)	6.6(5)	1.38(7)	0.89(364)
20537003	51079.53	0.69(2)	2.68(3)	1.27(4)	0.99(8)	3.37(1)	-0.12(4)	4.65(1)	6.5(2)	0.41(5)	1.2(234)

[†] The spectral model is $wabs * (blackbody + Comptb + Gaussian) * smedge$, where N_H is fixed at a value $3.00{\times}10^{21}$ cm^{-2} (Bloser et al., 2000); [††] normalization parameters of *blackbody* and *Comptb* components are in units of $10^{-2} \times L_{39}/d_{10}^2$ $erg/s/kpc^2$, where L_{39} is the source luminosity in units of 10^{39} erg/s, d_{10}^2 is the distance to the source in units of 10 kpc and *Gaussian* component is in units of $10^{-2} \times total$ $photons\ cm^{-2}s^{-1}$ in line, wherein σ_{line} of *Gaussian* component is fixed to a value 0.8 keV (see comments in the text); smeared edge included at 7.7 keV.

Table 4. Best-fit parameters of spectral analysis of PCA&HEXTE/*RXTE* observations of 4U 1820-30 in 3-200 keV energy range[†]. Parameter errors correspond to 90% confidence level.

Observational ID	MJD, day	$\alpha = \Gamma - 1$	T_e, keV	$\log(A)^{\dagger\dagger}$	$N_{COMPTB}^{\dagger\dagger\dagger}$	T_s, keV	$N_{Bbody}^{\dagger\dagger\dagger}$	E_{line}, keV	$N_{line}^{\dagger\dagger\dagger}$	χ^2_{red} (d.o.f.)	$F_1/F_2^{\dagger\dagger\dagger\dagger}$
10076-01-01-00	50151.937	1.00(2)	2.87(2)	$2.00^{\dagger\dagger}$	7.13(1)	1.30(5)	3.42(1)	6.27(8)	1.1(1)	1.54(78)	6.13/2.24
10074-01-01-00	50204.375	1.0(1)	2.93(4)	$2.00^{\dagger\dagger}$	5.5(2)	1.0(1)	2.31(3)	6.52(6)	0.15(3)	0.92(78)	4.58/1.61
10074-01-01-01	50204.511	0.99(2)	2.91(1)	$2.00^{\dagger\dagger}$	5.3(1)	1.08(2)	2.57(4)	6.5(1)	0.23(3)	0.93(78)	4.52/1.58
10074-01-01-02	50204.785	1.00(2)	2.95(2)	0.92(8)	5.25(9)	1.05(3)	2.48(6)	6.40(4)	0.14(2)	1.06(78)	4.33/1.53
10074-01-02-02	50207.381	1.00(5)	2.84(2)	0.9(1)	7.5(1)	1.06(5)	2.15(4)	6.58(4)	0.23(3)	1.09(78)	5.90/2.06
10074-01-02-00	50207.591	0.99(2)	2.86(1)	$2.00^{\dagger\dagger}$	7.74(2)	1.13(1)	2.46(7)	6.48(3)	0.32(5)	1.58(78)	6.29/2.37
10074-01-02-01	50207.927	0.99(3)	2.89(3)	$2.00^{\dagger\dagger}$	7.42(8)	1.06(4)	2.16(3)	6.38(5)	0.20(2)	0.87(78)	6.05/2.33
10076-01-02-00	50235.532	0.99(2)	2.89(2)	1.09(7)	4.91(1)	1.31(5)	1.96(1)	6.57(4)	0.22(2)	0.74(78)	4.05/1.43
10075-01-01-000	50371.943	1.00(2)	3.02(1)	$2.00^{\dagger\dagger}$	4.0(2)	1.07(2)	2.27(1)	6.49(3)	0.12(1)	1.63(78)	3.47/1.36
10075-01-01-010	50382.566	0.99(2)	3.09(2)	$2.00^{\dagger\dagger}$	3.66(3)	1.30(3)	2.03(2)	6.62(7)	0.14(1)	1.08(78)	3.16/1.30
10075-01-01-020	50384.633	0.96(9)	2.84(1)	$2.00^{\dagger\dagger}$	4.73(1)	1.31(5)	2.18(1)	6.53(4)	0.15(2)	1.24(78)	3.91/1.43
10075-01-01-031	50386.830	0.99(2)	2.89(2)	0.98(4)	5.43(4)	1.31(2)	2.18(2)	6.64(3)	0.23(3)	1.23(78)	4.43/1.58
20075-01-01-00	50488.426	1.01(2)	2.90(2)	$2.00^{\dagger\dagger}$	6.92(3)	1.30(8)	2.65(3)	6.56(2)	0.24(2)	0.74(78)	5.34/1.89
20075-01-02-00	50513.955	0.99(2)	2.85(1)	0.90(5)	7.99(4)	1.32(6)	2.58(5)	6.57(4)	0.29(4)	0.94(78)	6.29/2.19
20075-01-02-01	50514.001	1.00(1)	2.92(1)	$2.00^{\dagger\dagger}$	7.86(3)	1.11(2)	2.60(3)	6.51(3)	0.26(4)	0.94(78)	6.51/2.53
20075-01-03-01	50528.638	0.97(6)	2.92(5)	$2.00^{\dagger\dagger}$	5.05(2)	1.10(5)	2.73(4)	6.44(8)	0.17(5)	1.03(78)	4.27/1.54
20075-01-03-00	50530.705	0.95(1)	2.91(2)	0.65(5)	6.47(7)	1.11(3)	2.55(3)	6.60(3)	0.20(2)	0.94(78)	5.03/1.80
20075-01-04-00	50548.703	0.96(3)	2.95(1)	0.7(1)	5.53(5)	1.23(8)	2.49(2)	6.56(3)	0.18(2)	1.01(78)	3.90/1.44
20075-01-05-00	50570.585	0.99(2)	3.93(2)	0.8(1)	3.22(2)	1.10(2)	2.27(1)	6.90(6)	0.14(3)	1.01(78)	2.49/1.42
20075-01-05-01	50578.549	1.00(2)	2.84(4)	$2.00^{\dagger\dagger}$	6.42(4)	1.12(4)	2.29(2)	6.40(5)	0.38(4)	1.01(78)	5.23/1.86
20075-01-06-00	50595.327	0.99(3)	2.88(2)	1.03(4)	7.96(1)	1.11(6)	2.83(5)	6.54(3)	0.47(3)	1.01(78)	6.46/2.30
20075-01-06-01	50596.432	1.00(2)	2.83(3)	0.96(1)	8.49(1)	1.10(5)	2.73(3)	6.40(6)	0.45(3)	1.01(78)	6.75/2.36
20075-01-07-01	50622.760	1.01(2)	2.86(2)	0.97(4)	8.37(4)	1.11(7)	3.26(7)	6.50(3)	0.61(4)	1.01(78)	6.90/2.38
20075-01-07-00	50622.546	1.00(1)	2.86(2)	0.97(3)	8.31(3)	1.10(5)	3.24(6)	6.48(2)	0.63(4)	1.01(78)	6.86/2.36
20075-01-08-00	50645.216	1.00(2)	2.93(1)	$2.00^{\dagger\dagger}$	7.86(1)	1.10(9)	2.83(2)	6.44(3)	0.30(3)	1.01(78)	6.48/2.56
20075-01-08-01	50645.485	1.00(1)	2.91(1)	$2.00^{\dagger\dagger}$	6.37(4)	1.10(7)	2.73(7)	6.50(4)	0.40(5)	1.01(78)	5.33/1.89
20075-01-09-00	50675.454	0.99(1)	2.87(3)	0.67(2)	7.81(2)	1.12(8)	2.74(5)	6.52(5)	0.46(7)	1.01(78)	5.97/2.04

Table 4—Continued

Observational ID	MJD, day	$\alpha =$ $\Gamma - 1$	T_e, keV	$\log(A)^{\dagger\dagger}$	$N_{COMPTB}^{\dagger\dagger\dagger}$	T_s, keV	$N_{Bbody}^{\dagger\dagger\dagger}$	E_{line}, keV	$N_{line}^{\dagger\dagger\dagger}$	χ^2_{red} (d.o.f.)	$F_1/F_2^{\dagger\dagger\dagger\dagger}$
20075-01-10-00	50701.149	1.00(1)	2.92(2)	$2.00^{\dagger\dagger}$	4.90(3)	1.11(5)	2.91(1)	6.37(3)	0.41(4)	1.09(78)	4.35/1.56
20075-01-10-01	50701.251	1.00(2)	2.91(1)	$2.00^{\dagger\dagger}$	5.17(3)	1.10(6)	2.90(5)	6.37(3)	0.41(4)	1.09(78)	4.56/1.63
30057-01-01-01	50907.412	1.02(5)	3.00(2)	0.70(3)	4.51(1)	1.12(5)	2.40(1)	6.5(1)	0.31(1)	1.76(78)	3.63/1.32
30057-01-01-00	50908.660	1.00(1)	2.83(1)	1.02(1)	6.18(2)	1.11(2)	2.35(7)	6.41(9)	0.37(2)	1.20(78)	4.95/1.74
30057-01-01-02	50909.662	1.01(3)	2.95(1)	0.72(2)	5.06(3)	1.10(4)	2.58(5)	6.51(8)	0.29(2)	1.12(78)	4.05/1.45
30057-01-01-03	50910.589	1.00(1)	2.94(2)	0.66(2)	5.43(1)	1.12(5)	2.53(6)	6.6(1)	0.33(2)	0.79(78)	4.29/1.52
30057-01-01-04	50910.790	0.99(2)	2.87(2)	0.77(2)	6.20(3)	1.12(5)	2.64(7)	6.5(1)	0.32(1)	0.79(78)	4.74/1.68
30053-03-01-000	50920.197	0.99(4)	2.93(2)	$2.00^{\dagger\dagger}$	4.74(5)	1.10(2)	2.62(4)	6.54(2)	0.34(2)	0.57(78)	4.07/1.45
30053-03-02-00	51079.552	1.00(3)	2.91(1)	0.75(1)	6.42(1)	1.11(1)	2.84(2)	6.52(3)	0.36(3)	1.17(78)	5.06/1.83
30053-03-02-01	51079.719	1.00(2)	2.89(4)	0.73(1)	6.45(3)	1.10(5)	2.77(2)	6.51(4)	0.34(3)	1.19(78)	5.05/1.80
30053-03-02-04	51079.812	0.99(1)	2.86(2)	0.99(5)	5.97(1)	1.12(6)	2.84(2)	6.45(9)	0.77(1)	1.22(78)	4.97/1.76
30053-03-02-05	51079.879	0.9(1)	2.86(5)	0.41(3)	5.91(2)	1.11(4)	2.86(2)	6.65(6)	0.15(3)	0.90(78)	4.37/1.54
30053-03-02-02	51080.229	0.99(4)	2.99(1)	0.74(1)	4.59(1)	1.10(5)	2.63(1)	6.51(4)	0.19(2)	1.13(78)	3.73/1.35
30053-03-02-03	51080.413	1.00(3)	2.93(3)	$2.00^{\dagger\dagger}$	4.09(3)	1.11(2)	2.58(3)	6.42(5)	0.29(1)	1.17(78)	3.50/1.28
30057-01-02-00	51320.532	0.98(3)	2.96(3)	0.85(1)	5.28(4)	1.12(3)	3.43(7)	6.51(6)	0.31(3)	0.86(78)	4.71/1.59
30057-01-02-01	51321.713	1.00(1)	2.99(1)	0.72(3)	6.02(4)	1.10(4)	3.36(1)	6.5(1)	0.47(5)	0.84(78)	4.89/1.76
30057-01-02-02	51323.729	1.01(3)	2.93(1)	$2.00^{\dagger\dagger}$	4.92(3)	1.11(5)	3.47(1)	6.51(4)	0.33(1)	0.82(78)	4.20/1.53
30057-01-02-03	51324.378	1.00(1)	2.95(2)	0.92(3)	5.12(3)	1.12(2)	3.29(6)	6.42(6)	0.32(2)	1.24(78)	4.28/1.55
30057-01-02-05	51324.511	1.02(3)	2.94(1)	0.91(4)	5.03(2)	1.12(3)	3.33(5)	6.51(9)	0.33(1)	0.97(78)	4.23/1.52
30057-01-03-01	51410.501	1.00(3)	2.91(2)	0.84(3)	4.93(3)	1.13(2)	3.01(6)	6.57(8)	0.32(2)	0.98(78)	4.08/1.43
30057-01-03-02	51411.499	0.99(2)	2.94(1)	0.96(4)	4.63(4)	1.12(5)	3.01(1)	6.54(9)	0.35(2)	0.98(78)	3.89/1.41
30057-01-03-000	51412.315	1.02(4)	2.87(4)	0.91(4)	5.82(3)	1.12(4)	2.94(1)	6.51(5)	0.46(3)	1.50(78)	4.71/1.68
30057-01-04-12	51418.427	1.00(2)	2.83(3)	$2.00^{\dagger\dagger}$	3.84(7)	1.15(5)	2.83(7)	6.49(8)	0.30(4)	0.76(78)	3.42/1.21
30057-01-04-00	51418.557	0.98(3)	2.87(1)	$2.00^{\dagger\dagger}$	3.89(3)	1.14(2)	2.93(6)	6.48(9)	0.27(1)	1.10(78)	3.38/1.21
30057-01-04-01	51419.289	1.00(2)	2.93(1)	$2.00^{\dagger\dagger}$	3.54(1)	1.11(3)	2.48(2)	6.5(1)	0.29(2)	1.50(78)	3.06/1.17
30057-01-04-02	51419.427	1.00(1)	2.95(2)	$2.00^{\dagger\dagger}$	3.60(2)	1.12(2)	2.43(5)	6.43(4)	0.29(1)	0.86(78)	3.09/1.18
30057-01-04-03	51424.416	1.02(3)	2.91(1)	$2.00^{\dagger\dagger}$	3.77(2)	1.12(2)	2.49(5)	6.51(6)	0.27(2)	0.78(78)	3.19/1.17

Table 4—Continued

Observational ID	MJD, day	$\alpha = \Gamma - 1$	T_e, keV	$\log(A)^{\dagger\dagger}$	$N_{COMPTB}^{\dagger\dagger\dagger}$	T_s, keV	$N_{Bbody}^{\dagger\dagger\dagger}$	E_{line}, keV	$N_{line}^{\dagger\dagger\dagger}$	χ^2_{red} (d.o.f.)	$F_1/F_2^{\dagger\dagger\dagger\dagger}$
30057-01-04-04	51424.483	0.99(3)	2.93(1)	$2.00^{\dagger\dagger}$	3.75(3)	1.16(3)	2.50(5)	6.56(5)	0.28(3)	0.85(78)	3.18/1.18
30057-01-04-05	51432.379	1.00(1)	2.92(2)	0.88(4)	3.31(2)	1.11(4)	2.19(4)	6.51(1)	0.31(4)	0.75(78)	2.78/0.98
30057-01-04-06	51425.348	0.98(3)	2.93(2)	0.86(3)	4.53(3)	1.11(2)	2.39(5)	6.52(9)	0.36(1)	1.08(78)	3.68/1.34
30057-01-04-07G	51428.354	1.03(3)	2.89(1)	$2.00^{\dagger\dagger}$	2.91(2)	1.12(1)	1.87(3)	6.58(5)	0.24(4)	1.08(78)	2.47/0.91
30057-01-04-08G	51430.007	1.00(1)	2.89(1)	$2.00^{\dagger\dagger}$	2.91(2)	1.12(2)	1.87(3)	6.51(2)	0.24(5)	1.04(78)	2.47/0.91
30057-01-05-00	51435.001	0.99(1)	2.89(2)	0.61(4)	4.86(5)	1.14(5)	2.93(1)	6.56(3)	0.41(1)	1.18(78)	3.85/1.29
30057-01-04-09	51436.225	0.98(3)	2.93(1)	0.60(4)	4.77(4)	1.13(4)	2.81(3)	6.51(6)	0.35(1)	0.98(78)	3.75/1.29
30057-01-06-02	51466.231	1.00(2)	2.93(1)	1.02(7)	5.55(9)	1.12(2)	3.65(8)	6.47(3)	0.57(8)	1.46(78)	4.82/1.70
30057-01-06-03	51466.440	1.00(1)	2.91(1)	1.02(8)	5.83(9)	1.11(2)	3.71(9)	6.50(7)	0.53(7)	0.79(78)	4.99/1.72
30057-01-06-00	51466.499	0.97(3)	2.93(2)	0.97(7)	5.62(6)	1.11(5)	3.67(5)	6.55(6)	0.60(8)	1.18(78)	4.86/1.71
30057-01-06-04	51466.965	1.01(3)	2.91(1)	0.96(9)	6.18(8)	1.10(3)	3.95(9)	6.51(4)	0.75(9)	1.12(78)	5.35/1.85
30057-01-06-01	51467.035	1.00(1)	2.92(2)	0.84(8)	5.96(7)	1.12(3)	3.84(6)	6.52(6)	0.69(4)	0.69(78)	5.09/1.74
30057-01-06-05	51467.098	0.99(2)	2.96(2)	1.00(9)	5.54(1)	1.12(2)	3.89(9)	6.52(8)	0.54(8)	0.72(78)	4.83/1.72
40017-01-01-00	51206.852	1.01(3)	2.88(9)	1.08(3)	7.37(9)	1.20(4)	3.08(8)	6.50(4)	0.50(7)	0.81(78)	6.10/2.24
40017-01-01-02	51206.924	0.99(3)	2.93(5)	0.91(3)	7.40(8)	1.21(2)	2.98(9)	6.51(5)	0.90(9)	1.00(78)	6.01/2.22
40017-01-01-01	51207.002	1.00(2)	2.91(1)	$2.00^{\dagger\dagger}$	7.03(9)	1.13(3)	3.03(8)	6.52(7)	0.91(9)	0.90(78)	5.91/2.18
40017-01-01-03	51207.128	1.00(2)	2.94(2)	$2.00^{\dagger\dagger}$	6.96(9)	1.12(2)	3.06(7)	6.57(3)	0.36(4)	0.88(78)	5.83/2.15
40017-01-02-00	51222.642	0.98(3)	3.00(1)	$2.00^{\dagger\dagger}$	4.97(6)	1.14(5)	3.47(6)	6.54(7)	0.90(7)	1.30(78)	4.58/1.72
40017-01-03-00	51238.040	1.06(4)	2.90(3)	$2.00^{\dagger\dagger}$	3.23(7)	1.13(2)	2.31(4)	5.59(3)	0.16(5)	1.31(78)	2.82/1.05
40017-01-03-01	51238.242	1.02(3)	2.88(2)	$2.00^{\dagger\dagger}$	3.14(8)	1.12(4)	2.30(4)	6.15(6)	0.12(6)	1.21(78)	2.71/1.02
40017-01-04-00	51253.697	1.00(1)	2.97(1)	$2.00^{\dagger\dagger}$	4.62(3)	1.13(5)	2.60(5)	6.21(5)	0.24(7)	0.86(78)	3.98/1.49
40017-01-05-00	51268.750	1.00(2)	2.91(3)	$2.00^{\dagger\dagger}$	7.67(9)	1.12(2)	3.27(1)	6.18(7)	0.44(8)	1.09(78)	6.41/2.53
40017-01-06-00	51283.608	1.07(4)	2.88(2)	0.79(5)	9.98(6)	1.15(2)	3.93(3)	6.5(1)	0.59(6)	1.40(78)	7.89/2.81
40017-01-06-01	51283.768	1.04(3)	2.93(1)	$2.00^{\dagger\dagger}$	10.46(7)	1.13(1)	3.97(4)	6.4(1)	0.62(7)	1.24(78)	8.39/3.22
40017-01-05-01	51296.888	1.01(3)	2.91(2)	0.78(4)	7.71(8)	1.12(5)	2.99(2)	6.21(6)	0.46(5)	1.03(78)	6.02/2.21
40017-01-07-01	51300.010	1.00(2)	2.89(2)	0.92(6)	11.61(8)	1.12(2)	5.07(2)	6.41(9)	2.19(6)	1.04(78)	9.52/3.39
40017-01-07-00	51300.067	1.00(1)	2.94(1)	0.70(8)	10.35(9)	1.14(5)	4.58(3)	6.27(5)	1.72(8)	1.51(78)	8.31/2.93

Table 4—Continued

Observational ID	MJD, day	$\alpha = \Gamma - 1$	T_e, keV	log$(A)^{\dagger\dagger}$	$N_{COMPTB}^{\dagger\dagger\dagger}$	T_s, keV	$N_{Bbody}^{\dagger\dagger\dagger}$	E_{line}, keV	$N_{line}^{\dagger\dagger\dagger}$	χ^2_{red} (d.o.f.)	$F_1/F_2^{\dagger\dagger\dagger\dagger}$
40017-01-08-00	51313.655	1.01(3)	2.95(2)	0.87(3)	6.93(9)	1.13(2)	3.62(1)	6.49(7)	1.20(1)	1.04(78)	5.79/2.09
40017-01-09-00	51330.505	1.00(1)	2.90(1)	0.79(2)	8.12(5)	1.14(3)	3.65(1)	6.41(4)	1.21(2)	1.03(78)	6.51/2.32
40017-01-10-00	51343.836	1.00(2)	2.90(2)	1.00(3)	7.79(8)	1.11(2)	3.60(1)	6.43(6)	1.52(7)	1.06(78)	6.62/2.42
40017-01-10-01	51343.901	0.99(7)	2.91(2)	0.9(1)0	7.37(9)	1.12(3)	3.76(9)	6.51(3)	0.46(4)	1.50(78)	6.13/2.17
40017-01-10-02	51343.968	0.99(3)	2.87(1)	1.07(9)	7.88(6)	1.14(1)	3.68(2)	6.59(7)	1.29(5)	1.24(78)	6.60/2.36
40017-01-11-01	51355.422	1.00(1)	2.95(2)	0.95(1)	6.13(6)	1.15(5)	3.06(1)	6.5(1)	0.33(5)	0.88(78)	5.13/1.90
40017-01-11-02	51355.489	1.00(2)	2.93(2)	0.97(3)	6.87(8)	1.12(2)	2.93(2)	6.63(7)	0.35(4)	1.09(78)	5.64/2.11
40017-01-11-00	51355.562	0.99(2)	2.94(1)	0.92(3)	6.56(7)	1.13(1)	2.98(1)	6.53(6)	0.37(7)	1.00(78)	5.37/1.99
40017-01-12-00	51389.381	0.99(3)	2.94(1)	2.00††	7.80(6)	1.13(2)	3.29(1)	6.24(3)	0.63(2)	1.10(78)	6.48/2.63
40017-01-11-03	51495.992	0.98(3)	2.95(2)	0.74(2)	7.31(5)	1.12(4)	4.58(3)	6.38(6)	0.56(3)	1.00(78)	6.41/2.19
40017-01-12-01	51496.185	1.00(3)	2.99(1)	0.72(2)	7.25(6)	1.14(5)	4.42(2)	6.21(8)	0.59(1)	1.47(78)	6.29/2.20
40017-01-13-00	51400.444	1.00(2)	2.94(1)	0.79(4)	7.59(4)	1.13(2)	3.13(1)	6.58(2)	0.41(2)	1.20(78)	6.00/2.23
40017-01-14-00	51407.503	1.02(3)	2.92(2)	0.82(3)	5.68(4)	1.12(5)	2.85(2)	6.5(2)	0.34(2)	1.17(78)	4.71/1.71
40017-01-15-00	51417.295	1.01(2)	3.00(1)	0.97(2)	4.69(3)	1.14(3)	2.69(2)	6.4(1)	0.27(4)	1.39(78)	3.92/1.47
40019-02-01-00	51421.302	1.00(1)	2.97(2)	2.00††	3.82(8)	1.12(2)	2.19(1)	6.57(1)	0.14(5)	1.35(78)	3.31/1.27
40019-02-01-03	51421.635	0.98(4)	3.01(1)	2.00††	3.77(4)	1.11(2)	2.19(1)	6.61(5)	0.19(5)	0.86(78)	3.29/1.29
40019-02-01-04	51421.707	1.00(2)	2.99(1)	2.00††	6.84(3)	1.11(3)	2.09(1)	6.84(3)	0.12(3)	1.28(78)	3.23/1.26
40019-02-01-10	51421.777	1.01(3)	2.97(3)	2.00††	3.87(4)	1.12(4)	2.40(3)	6.75(2)	0.19(1)	1.15(78)	3.39/1.29
40019-02-01-11	51421.846	1.00(2)	2.97(2)	2.00††	3.85(3)	1.13(5)	2.37(1)	6.53(4)	0.13(4)	0.73(78)	3.37/1.28
40019-02-01-01	51421.952	0.98(3)	3.00(2)	2.00††	3.56(3)	1.12(2)	2.20(2)	6.67(3)	0.13(4)	0.86(78)	3.12/1.21
40019-02-01-02G	51422.083	0.99(3)	3.10(3)	2.00††	3.51(4)	1.12(3)	1.96(1)	7.36(6)	0.62(3)	0.79(78)	3.03/1.26
40019-02-01-05G	51422.257	1.01(3)	2.97(2)	2.00††	3.89(3)	1.13(2)	2.33(3)	6.51(4)	0.19(4)	0.91(78)	3.40/1.29
40019-02-01-06	51422.561	1.01(3)	2.98(2)	2.00††	3.72(2)	1.11(5)	2.35(1)	6.51(6)	0.15(3)	0.84(78)	3.27/1.24
40019-02-01-07	51422.634	0.97(6)	2.97(1)	2.00††	3.73(4)	1.12(2)	2.30(1)	6.59(8)	0.14(2)	0.89(78)	3.26/1.24
40019-02-01-09	51422.706	1.00(1)	2.92(1)	2.00††	3.72(3)	1.12(3)	2.34(1)	6.51(3)	0.16(3)	1.34(78)	3.49/1.29
40017-01-16-00G	51429.075	1.04(5)	2.95(1)	2.00††	3.19(2)	1.12(5)	1.96(1)	6.62(5)	0.43(6)	1.28(78)	1.03/1.47
40017-01-17-00	51440.060	0.98(3)	2.97(2)	0.58(9)	4.85(3)	1.14(4)	2.52(2)	6.70(9)	0.69(2)	1.02(78)	3.81/1.35

Table 4—Continued

Observational ID	MJD, day	$\alpha = \Gamma - 1$	T_e, keV	$\log(A)^{\dagger\dagger}$	$N_{COMPTB}^{\dagger\dagger\dagger}$	T_s, keV	$N_{Bbody}^{\dagger\dagger\dagger}$	E_{line}, keV	$N_{line}^{\dagger\dagger\dagger}$	χ^2_{red} (d.o.f.)	$F_1/F_2^{\dagger\dagger\dagger\dagger}$
40017-01-17-01	51440.218	1.00(1)	2.89(2)	0.65(8)	5.22(3)	1.12(3)	2.53(1)	6.52(8)	0.89(1)	1.28(78)	4.13/1.42
40017-01-18-00	51464.368	0.99(3)	2.97(1)	$2.00^{\dagger\dagger}$	5.47(9)	1.13(2)	3.54(2)	6.18(7)	1.08(3)	1.28(78)	4.84/1.79
40017-01-19-00	51480.115	0.97(3)	2.90(1)	0.91(3)	10.98(7)	1.13(3)	4.03(1)	6.46(9)	2.15(4)	0.96(78)	8.79/3.25
40017-01-20-00	51495.667	1.00(1)	2.92(2)	$2.00^{\dagger\dagger}$	7.13(8)	1.14(5)	4.66(2)	6.23(6)	1.93(8)	0.89(78)	8.67/2.22
40017-01-19-01	51496.326	1.00(2)	3.06(2)	0.67(2)	6.97(4)	1.12(3)	4.22(3)	6.85(5)	1.34(5)	0.57(78)	6.02/2.21
40017-01-19-02	51496.395	1.01(3)	2.92(1)	1.06(9)	7.05(5)	1.12(2)	4.47(1)	6.34(7)	1.84(7)	0.98(78)	6.38/2.18
40017-01-20-01	51496.666	0.98(3)	2.98(2)	0.65(9)	8.16(5)	1.14(5)	4.32(1)	6.50(8)	1.55(6)	0.91(78)	6.73/2.34
40017-01-21-00	51941.015	1.00(1)	2.99(4)	0.97(4)	4.05(7)	1.13(4)	1.93(2)	6.22(9)	0.67(9)	0.89(78)	3.43/1.32
40017-01-21-01	51941.240	1.00(3)	3.00(1)	0.80(4)	4.24(3)	1.12(3)	1.77(1)	6.63(4)	0.65(4)	1.04(78)	3.35/1.04
40017-01-21-02	51941.303	0.99(2)	2.96(4)	1.09(5)	3.94(8)	1.11(2)	1.77(1)	6.34(6)	0.64(3)	0.82(78)	3.22/1.00
40017-01-22-00	51955.872	0.99(3)	3.03(1)	0.93(4)	4.73(3)	1.12(1)	2.38(2)	6.32(9)	0.68(6)	1.07(78)	3.94/1.55
40017-01-22-01	51956.009	1.00(2)	3.02(1)	0.96(4)	4.40(3)	1.15(5)	2.26(2)	6.09(5)	0.92(4)	1.11(78)	3.77/1.49
60030-01-01-00	51996.856	1.00(3)	2.97(1)	0.89(4)	10.20(8)	1.12(4)	3.68(3)	6.32(2)	0.56(5)	1.26(78)	8.17/3.03
60030-01-01-01G	51997.785	1.01(2)	2.96(2)	$2.00^{\dagger\dagger}$	13.5(1)	1.14(5)	3.19(2)	6.14(5)	0.74(6)	1.40(78)	10.84/4.49
60030-01-01-02G	51997.851	0.99(3)	2.88(1)	$2.00^{\dagger\dagger}$	12.54(9)	1.12(3)	4.04(5)	6.36(3)	0.78(8)	0.95(78)	10.07/3.71
60030-01-01-03	51997.918	1.00(2)	2.92(1)	$2.00^{\dagger\dagger}$	13.5(1)	1.13(5)	3.05(2)	6.16(4)	0.69(2)	1.26(78)	10.71/4.29
60030-01-02-00	51998.911	0.99(3)	2.94(2)	$2.00^{\dagger\dagger}$	11.72(9)	1.11(2)	3.26(3)	6.38(5)	0.64(3)	1.49(78)	9.29/3.58
60030-01-02-01	51999.642	1.02(2)	2.94(1)	0.92(3)	11.62(8)	1.11(1)	3.45(2)	6.54(3)	0.69(4)	1.17(78)	9.19/3.41
60030-01-02-02	51999.707	1.01(3)	2.94(1)	0.84(4)	11.31(8)	1.12(3)	3.43(2)	6.54(7)	0.62(3)	0.77(78)	8.90/3.25
40017-01-23-00	52355.020	1.00(1)	2.92(2)	0.98(2)	9.48(7)	1.13(5)	4.37(4)	6.31(8)	2.13(3)	1.21(78)	8.21/3.26
40017-01-23-01	52355.883	1.01(3)	2.91(1)	$2.00^{\dagger\dagger}$	10.06(6)	1.53(6)	4.90(1)	6.46(7)	2.14(5)	1.31(78)	11.91/3.55
40017-01-24-00	52429.708	1.01(3)	9.94(9)	0.13(5)	2.32(2)	1.69(3)	1.16(2)	6.80(8)	0.50(1)	1.00(78)	1.50/1.62
70030-03-02-00	52478.468	1.02(5)	2.92(3)	$2.00^{\dagger\dagger}$	6.59(4)	1.12(4)	2.81(1)	6.27(5)	0.52(6)	1.25(78)	5.52/2.09
70030-03-02-000	52478.137	1.01(3)	2.93(1)	$2.00^{\dagger\dagger}$	6.34(6)	1.14(5)	2.75(1)	6.22(3)	0.43(4)	0.82(78)	5.20/2.02
70030-03-02-01	52479.406	1.01(2)	3.00(2)	$2.00^{\dagger\dagger}$	6.00(5)	1.13(4)	3.09(3)	6.11(3)	0.51(2)	1.13(78)	4.83/1.85
70030-03-02-020	52480.254	1.01(3)	2.94(1)	$2.00^{\dagger\dagger}$	7.48(6)	1.11(2)	2.76(1)	6.18(4)	0.34(3)	1.46(78)	6.18/2.46
70030-03-02-03G	52480.067	0.99(3)	2.94(1)	$2.00^{\dagger\dagger}$	6.47(4)	1.12(3)	2.39(3)	6.17(5)	0.29(2)	1.25(78)	5.35/2.13

Table 4—Continued

Observational ID	MJD, day	$\alpha = \Gamma - 1$	T_e, keV	$\log(A)^{\dagger\dagger}$	$N_{COMPTB}^{\dagger\dagger\dagger}$	T_s, keV	$N_{Bbody}^{\dagger\dagger\dagger}$	E_{line}, keV	$N_{line}^{\dagger\dagger\dagger}$	χ^2_{red} (d.o.f.)	$F_1/F_2^{\dagger\dagger\dagger\dagger}$
70030-03-02-03G	52480.067	1.00(1)	2.94(1)	$2.00^{\dagger\dagger}$	6.47(6)	1.11(2)	2.39(2)	6.18(3)	0.29(3)	1.21(78)	5.35/2.13
70030-03-01-01G	52480.182	0.99(4)	2.93(1)	$2.00^{\dagger\dagger}$	6.63(6)	1.11(4)	2.96(1)	6.25(4)	0.52(4)	1.30(78)	5.56/2.09
70030-03-01-00G	52482.158	1.01(3)	2.90(3)	$2.00^{\dagger\dagger}$	7.81(7)	1.14(5)	3.08(1)	6.14(8)	0.65(2)	1.18(78)	6.52/2.50
70030-03-01-02	52484.157	1.00(1)	2.89(1)	$2.00^{\dagger\dagger}$	8.15(8)	1.13(4)	3.07(2)	6.31(3)	0.54(6)	1.51(78)	6.67/2.47
70030-03-01-03	52487.171	1.00(3)	2.93(4)	$2.00^{\dagger\dagger}$	8.33(6)	1.15(6)	3.08(2)	6.17(2)	0.66(4)	0.86(78)	6.88/2.66
70030-03-03-00	52489.217	1.00(2)	2.90(2)	$2.00^{\dagger\dagger}$	8.30(7)	1.13(2)	3.02(3)	6.13(5)	0.73(3)	0.77(78)	6.87/2.64
70030-03-04-00	52801.149	0.99(3)	5.56(5)	$2.00^{\dagger\dagger}$	2.14(3)	1.12(1)	0.63(1)	6.64(2)	0.19(2)	0.74(78)	1.63/1.46
70030-03-04-01	52802.070	1.00(2)	5.79(3)	0.89(4)	2.35(2)	1.12(2)	0.95(1)	6.65(3)	0.09(1)	1.04(78)	1.63/1.49
70030-03-05-00	52804.043	1.02(3)	5.75(4)	0.90(2)	2.55(1)	1.11(2)	1.40(2)	6.65(2)	0.04(2)	1.19(78)	1.76/1.61
70030-03-05-01	52805.819	1.01(2)	5.34(4)	$2.00^{\dagger\dagger}$	2.99(6)	1.11(1)	1.28(1)	6.57(1)	0.14(3)	1.17(78)	2.11/1.84
70030-03-05-02	52806.937	1.01(3)	4.17(3)	$2.00^{\dagger\dagger}$	3.17(3)	1.12(3)	2.04(2)	5.64(4)	0.53(1)	1.20(78)	2.56/1.68
70030-03-05-03	52808.057	1.03(4)	3.05(2)	$2.00^{\dagger\dagger}$	4.61(2)	1.14(5)	3.01(3)	6.08(7)	0.36(5)	1.44(78)	4.04/1.64
70030-03-05-04	52808.978	1.01(2)	3.06(4)	$2.00^{\dagger\dagger}$	4.61(1)	1.13(4)	2.88(2)	6.40(4)	0.22(4)	1.02(78)	4.04/1.66
70030-03-07-03	54126.393	1.00(2)	3.00(1)	$2.00^{\dagger\dagger}$	4.43(3)	1.15(7)	3.34(2)	6.17(2)	0.65(4)	1.33(78)	4.02/1.53
70030-03-07-01	54127.244	1.00(1)	2.94(1)	$2.00^{\dagger\dagger}$	5.99(1)	1.11(2)	3.56(6)	6.04(1)	1.14(7)	1.22(78)	5.15/1.94
70030-03-07-00	54128.226	1.02(3)	3.00(5)	$2.00^{\dagger\dagger}$	6.78(4)	1.12(1)	3.28(3)	6.30(3)	0.59(1)	0.75(78)	5.66/2.35
70030-03-07-020	54129.013	1.01(2)	2.96(2)	$2.00^{\dagger\dagger}$	5.63(2)	1.12(3)	3.50(2)	6.04(2)	1.13(6)	0.85(78)	5.15/1.94
70031-05-01-00	52439.556	1.01(3)	6.87(2)	0.26(2)	2.77(1)	1.72(2)	2.25(2)	6.14(3)	1.67(7)	1.26(78)	4.02/1.50
80105-07-01-00	52894.237	1.00(1)	3.22(4)	0.19(3)	6.46(9)	1.66(3)	2.25(2)	6.16(2)	1.86(5)	1.12(78)	5.08/1.95
90027-01-01-00	53258.915	1.00(2)	3.11(2)	0.68(3)	3.54(4)	1.40(3)	2.67(2)	6.40(1)	0.02(2)	0.75(78)	2.89/1.19
90027-01-01-01	53259.704	1.00(3)	3.20(3)	0.52(4)	3.41(3)	1.41(2)	2.01(1)	6.41(3)	0.01(1)	1.28(78)	2.59/1.09
90027-01-01-03	53261.935	0.96(4)	3.12(3)	0.33(4)	5.81(6)	1.45(4)	2.67(4)	6.46(2)	0.02(1)	1.11(78)	4.23/1.63
90027-01-01-04	53262.921	1.01(3)	3.22(2)	0.34(3)	5.21(5)	1.39(3)	2.93(2)	6.42(6)	0.06(2)	0.91(78)	4.23/1.53
90027-01-01-05	53263.249	1.00(2)	3.17(2)	0.27(4)	6.12(6)	1.40(5)	2.74(2)	6.49(1)	0.01(1)	1.36(78)	4.43/1.69
90027-01-01-06	53264.495	0.99(3)	3.16(2)	0.32(3)	6.33(5)	1.42(4)	2.85(3)	6.42(5)	0.02(2)	1.15(78)	4.59/1.79
90027-01-02-00	53265.745	1.00(1)	3.12(2)	0.40(3)	7.15(6)	1.46(3)	2.93(2)	6.43(7)	0.03(2)	1.04(78)	5.14/2.08
90027-01-02-01	53266.336	0.99(3)	3.10(1)	0.37(5)	6.43(6)	1.38(2)	2.76(3)	6.42(1)	0.01(1)	1.12(78)	4.65/1.83

Table 4—Continued

Observational ID	MJD, day	$\alpha = \Gamma - 1$	T_e, keV	$\log(A)^{\dagger\dagger}$	$N_{COMPTB}^{\dagger\dagger\dagger}$	T_s, keV	$N_{Bbody}^{\dagger\dagger\dagger}$	E_{line}, keV	$N_{line}^{\dagger\dagger\dagger}$	χ^2_{red} (d.o.f.)	$F_1/F_2^{\dagger\dagger\dagger\dagger}$
90027-01-02-07	53266.727	0.99(3)	3.12(2)	0.40(6)	7.15(7)	1.41(4)	2.93(6)	6.40(3)	0.01(1)	0.87(78)	5.14/2.09
90027-01-02-08	53267.587	1.00(1)	3.08(2)	0.39(4)	6.38(6)	1.43(3)	2.68(8)	6.54(2)	0.03(1)	1.08(78)	4.60/1.82
90027-01-02-03	53268.372	1.01(2)	3.09(1)	0.38(4)	5.65(5)	1.40(1)	2.47(2)	6.41(3)	0.01(1)	1.04(78)	4.09/1.61
90027-01-02-04	53269.289	1.00(1)	3.17(2)	0.35(3)	4.97(4)	1.40(2)	2.47(2)	6.40(4)	0.02(3)	1.29(78)	3.66/1.45
90027-01-02-05	53270.860	0.98(5)	3.15(3)	0.32(1)	6.03(5)	1.42(3)	2.47(8)	6.40(3)	0.03(2)	0.89(78)	4.33/1.71
90027-01-02-06	53271.594	1.00(2)	3.12(2)	0.59(3)	6.13(6)	1.37(2)	2.65(8)	6.44(1)	0.02(1)	0.85(78)	4.46/1.95
90027-01-03-07	53272.498	1.00(2)	3.13(2)	0.32(4)	5.85(6)	1.39(3)	2.61(6)	6.69(5)	0.01(1)	1.04(78)	4.24/1.64
90027-01-03-08	53272.697	0.98(4)	3.08(3)	0.55(4)	5.98(4)	1.41(2)	2.54(8)	6.40(3)	0.02(2)	1.24(78)	4.34/1.84
90027-01-03-00	53273.491	1.01(2)	3.14(4)	0.46(3)	5.70(6)	1.40(1)	2.45(7)	6.69(1)	0.02(1)	0.93(78)	4.14/1.73
90027-01-03-09	53273.561	1.02(3)	3.09(2)	0.41(3)	5.58(5)	1.45(2)	2.32(6)	6.42(4)	0.01(1)	1.17(78)	4.03/1.62
90027-01-03-02	53274.206	1.00(2)	3.16(1)	0.34(6)	4.62(6)	1.42(2)	2.35(4)	6.40(4)	0.01(1)	1.05(78)	3.41/1.33
90027-01-03-01	53274.486	1.01(3)	3.24(2)	0.41(2)	3.71(4)	1.41(1)	2.06(8)	6.41(1)	0.02(1)	1.26(78)	2.78/1.15
90027-01-03-10	53274.759	1.04(4)	3.12(4)	0.51(3)	3.40(3)	1.41(2)	2.23(7)	6.57(8)	0.01(1)	1.08(78)	2.65/1.05
90027-01-03-11	53274.796	1.00(2)	3.12(3)	0.49(2)	3.39(3)	1.44(1)	2.06(2)	6.40(2)	0.02(2)	0.96(78)	2.59/1.04
90027-01-03-03	53275.520	0.99(3)	3.09(2)	0.56(4)	3.42(3)	1.43(2)	2.10(8)	6.43(1)	0.03(2)	1.13(78)	2.62/1.06
90027-01-03-04	53276.113	0.96(5)	3.21(3)	0.50(2)	3.68(6)	1.42(2)	2.25(4)	6.40(3)	0.01(1)	1.07(78)	2.82/1.17
90027-01-03-05	53277.419	1.00(1)	4.03(4)	0.53(3)	3.12(4)	1.40(3)	1.59(5)	6.41(6)	0.02(1)	1.10(78)	2.32/1.35
90027-01-03-06	53278.404	1.01(3)	3.35(3)	0.54(5)	3.64(5)	1.41(2)	2.15(8)	6.42(1)	0.01(1)	1.12(78)	2.77/1.26
90027-01-04-00	53279.267	1.01(2)	3.24(2)	0.30(4)	5.59(6)	1.40(2)	2.76(3)	6.43(4)	0.02(1)	0.97(78)	4.10/1.63
90027-01-04-05	53280.437	1.01(3)	3.09(4)	0.44(3)	4.1(1)	1.64(5)	2.68(4)	6.40(1)	0.09(5)	1.26(78)	3.25/1.31
90027-01-04-01	53281.354	1.02(3)	3.21(2)	0.42(2)	4.53(4)	1.41(2)	2.77(3)	6.40(1)	0.01(1)	0.99(78)	3.45/1.39
90027-01-04-03	53282.272	0.99(3)	3.27(2)	0.32(2)	4.91(6)	1.40(3)	2.73(5)	6.41(4)	0.02(2)	1.06(78)	3.67/1.47
90027-01-04-04	53283.127	1.00(2)	3.13(2)	0.27(1)	5.82(7)	1.42(2)	2.63(2)	6.43(7)	0.01(1)	0.98(78)	4.22/1.58
90027-01-04-02	53283.978	1.00(1)	3.16(1)	0.32(3)	6.08(5)	1.41(2)	2.72(4)	6.46(3)	0.03(1)	0.98(78)	4.41/1.74
90027-01-05-00	53286.080	0.99(4)	3.06(2)	0.9(1)	4.1(1)	1.25(3)	2.42(2)	6.24(5)	0.08(3)	1.16(78)	3.36/1.33
90027-01-06-00	53591.287	1.00(3)	15.06(7)	0.2(1)	2.72(5)	1.65(4)	1.34(1)	6.58(4)	1.43(4)	1.04(78)	1.55/2.09
91435-01-01-00	53692.085	0.99(4)	3.9(1)	-0.4(1)	11.33(9)	1.71(5)	6.49(7)	6.52(4)	0.96(2)	1.20(78)	8.76/3.61

Table 4—Continued

Observational ID	MJD, day	$\alpha = \Gamma - 1$	T_e, keV	$\log(A)^{\dagger\dagger}$	$N_{COMPTB}^{\dagger\dagger\dagger}$	T_s, keV	$N_{Bbody}^{\dagger\dagger\dagger}$	E_{line}, keV	$N_{line}^{\dagger\dagger\dagger}$	χ^2_{red} (d.o.f.)	$F_1/F_2^{\dagger\dagger\dagger\dagger}$
91435-01-01-01	53693.074	0.97(5)	3.8(1)	-0.37(9)	9.80(7)	1.70(2)	6.26(8)	6.45(5)	0.81(3)	0.99(78)	7.92/2.99
91435-01-01-02	53693.986	1.00(1)	4.2(2)	-0.6(1)	9.91(8)	1.69(3)	6.32(8)	6.46(4)	0.90(1)	0.79(78)	7.97/3.08
92030-02-01-00	53921.301	1.01(2)	3.03(2)	$2.00^{\dagger\dagger}$	7.71(7)	1.72(7)	4.31(4)	6.41(7)	0.90(2)	1.12(78)	6.41/2.37
92030-02-02-000	53921.366	1.01(3)	2.96(1)	$2.00^{\dagger\dagger}$	8.38(9)	0.99(2)	3.69(3)	6.45(4)	0.89(1)	1.14(78)	7.01/2.59
92030-02-03-02	53939.313	1.00(1)	3.05(3)	$2.00^{\dagger\dagger}$	6.65(6)	0.97(3)	4.75(1)	6.45(3)	0.97(6)	1.20(78)	5.73/2.23
92030-02-03-00	53939.439	1.00(2)	2.99(1)	$2.00^{\dagger\dagger}$	6.94(5)	0.98(4)	3.17(3)	6.47(4)	0.90(1)	0.95(78)	5.85/2.23
92030-02-03-01	53939.875	1.01(4)	3.02(2)	$2.00^{\dagger\dagger}$	6.05(7)	0.99(2)	2.53(5)	6.46(5)	0.91(2)	1.16(78)	5.26/1.98
92030-02-11-000	53953.255	1.00(2)	3.00(2)	$2.00^{\dagger\dagger}$	5.37(9)	0.83(4)	2.81(2)	6.86(2)	0.94(1)	1.00(78)	4.68/1.82
91151-04-01-00	53959.950	1.01(3)	3.10(2)	0.27(2)	6.78(5)	1.75(5)	3.74(6)	6.45(4)	1.03(7)	1.07(78)	5.32/2.06
91151-04-02-00	54028.232	1.01(4)	3.53(3)	-0.07(9)	9.86(7)	1.86(3)	5.51(8)	6.49(6)	0.90(1)	1.12(78)	7.65/2.96
92030-02-04-00	54125.301	1.03(5)	3.12(2)	$2.00^{\dagger\dagger}$	4.32(3)	0.99(8)	4.15(2)	4.85(4)	0.90(2)	1.06(78)	3.89/1.54
92030-02-05-00	54256.402	1.00(1)	3.07(1)	$2.00^{\dagger\dagger}$	4.24(2)	0.99(4)	3.37(3)	6.85(6)	0.87(7)	1.14(78)	3.81/1.50
92030-02-06-00	54257.346	0.99(4)	3.15(8)	$2.00^{\dagger\dagger}$	4.25(6)	0.83(7)	2.32(1)	5.99(7)	0.90(5)	1.21(78)	3.79/1.47
92030-02-06-01	54257.452	1.01(2)	3.16(2)	$2.00^{\dagger\dagger}$	4.22(4)	0.82(5)	2.31(1)	6.85(3)	0.88(2)	1.10(78)	3.91/1.52
92030-02-07-00	54258.447	1.04(4)	3.06(8)	$2.00^{\dagger\dagger}$	5.35(5)	0.81(3)	2.30(2)	6.81(5)	0.78(2)	0.79(78)	4.79/1.80
92030-02-10-00	54297.188	1.02(3)	3.15(2)	$2.00^{\dagger\dagger}$	3.74(3)	0.80(4)	2.31(2)	6.85(3)	0.95(3)	1.01(78)	3.58/1.44
92030-02-09-00	54306.346	1.00(1)	3.06(8)	$2.00^{\dagger\dagger}$	5.35(6)	0.84(2)	2.30(3)	6.82(4)	0.91(4)	1.15(78)	3.45/1.36
94090-01-01-00	54947.682	1.02(3)	11.09(4)	-0.35(5)	2.98(3)	0.83(3)	1.79(2)	5.83(5)	2.83(3)	1.21(78)	2.01/1.63
94090-01-01-01	54947.939	1.00(2)	10.28(5)	-0.34(4)	2.79(2)	0.82(4)	1.78(3)	5.65(4)	2.89(1)	1.04(78)	1.94/1.62
94090-01-01-02	54948.728	1.03(4)	10.31(4)	-0.36(6)	2.75(1)	0.86(3)	1.79(4)	6.45(5)	2.83(2)	1.18(78)	1.89/1.66
94090-01-01-03	54948.987	0.99(3)	10.61(6)	-0.17(5)	2.66(1)	0.89(2)	1.78(6)	6.46(4)	2.82(1)	1.04(78)	1.76/1.77
94090-01-01-04	54949.708	1.01(2)	10.12(3)	-0.05(5)	3.00(2)	0.81(4)	1.79(5)	6.47(3)	2.83(3)	1.09(78)	1.89/1.73
94090-01-01-05	54950.686	1.00(1)	10.01(4)	-0.16(4)	2.65(1)	0.80(3)	1.76(9)	6.45(2)	2.85(2)	1.03(78)	1.69/1.79
94090-01-02-00	54956.589	1.02(3)	17.80(7)	0.12(1)	2.83(1)	1.78(5)	1.43(1)	6.35(4)	1.10(1)	1.09(78)	1.58/2.14
94090-01-02-03	54956.769	1.01(4)	16.44(7)	0.11(1)	2.75(2)	1.57(2)	1.44(1)	6.31(4)	1.12(3)	1.17(78)	1.59/2.08
94090-01-02-04	54957.489	1.00(2)	16.92(8)	0.27(2)	2.67(1)	1.62(3)	1.43(3)	6.38(5)	1.19(2)	1.09(78)	1.52/2.05
94090-01-02-01	54957.626	1.03(4)	17.31(9)	0.21(3)	2.61(1)	1.57(4)	1.41(2)	6.37(8)	1.11(2)	1.08(78)	1.50/2.00

Table 4—Continued

Observational ID	MJD, day	$\alpha = \Gamma - 1$	T_e, keV	log$(A)^{\dagger\dagger}$	$N^{\dagger\dagger\dagger}_{COMPTB}$	T_s, keV	$N^{\dagger\dagger\dagger}_{Bbody}$	E_{line}, keV	$N^{\dagger\dagger\dagger}_{line}$	χ^2_{red} (d.o.f.)	$F_1/F_2^{\dagger\dagger\dagger\dagger}$
94090-01-02-02	54958.664	1.00(2)	20.47(9)	0.01(2)	2.69(2)	1.69(3)	1.40(5)	6.34(4)	1.16(2)	1.10(78)	1.49/2.08
94090-01-03-00	54960.585	0.97(5)	20.3(1)	0.01(1)	2.56(1)	1.56(2)	1.44(8)	6.34(5)	1.10(9)	1.04(78)	1.41/2.00
94090-01-04-00	54978.287	1.00(2)	12.54(9)	0.47(4)	3.04(1)	1.43(6)	1.43(2)	6.36(4)	3.07(3)	1.10(78)	1.78/2.60
94090-01-04-01	54978.485	1.01(3)	11.32(4)	0.56(9)	3.04(5)	1.39(2)	1.44(3)	6.33(3)	3.08(2)	1.49(78)	1.80/2.63
94090-01-04-02	54978.749	0.99(2)	12.51(4)	0.67(8)	2.94(3)	1.73(9)	1.45(1)	6.38(4)	3.01(6)	0.99(78)	1.72/2.68
94090-01-04-03	54979.271	1.00(1)	14.96(5)	0.47(3)	2.87(2)	1.71(8)	1.43(2)	6.48(6)	3.07(4)	0.97(78)	1.67/2.56
94090-01-05-01	54980.781	1.00(3)	14.34(5)	0.54(9)	3.04(4)	1.40(2)	0.53(1)	6.42(2)	1.08(5)	0.96(78)	1.96/2.60
94090-01-05-00	54981.669	1.02(4)	13.25(4)	0.56(7)	3.15(5)	1.53(4)	1.44(2)	6.39(4)	3.14(9)	0.98(78)	1.84/2.76
94090-02-01-00	54994.514	0.97(4)	8.13(5)	-0.08(4)	4.72(5)	1.40(5)	2.54(3)	6.41(4)	1.06(7)	0.96(78)	3.18/2.96
94090-02-01-01	54997.718	1.00(2)	3.09(2)	0.42(5)	8.48(9)	1.41(2)	5.46(5)	6.45(3)	0.90(5)	0.93(78)	6.78/2.47
94090-02-02-00	55002.625	0.99(4)	3.12(2)	0.41(3)	8.98(7)	1.40(2)	6.46(7)	6.46(2)	0.91(2)	0.96(78)	6.99/2.65
92030-02-12-00	55080.709	1.01(2)	2.98(3)	2.00††	7.18(9)	0.83(5)	4.11(4)	6.86(6)	0.87(3)	1.19(78)	6.13/2.38
92030-02-12-01	55082.884	1.00(1)	3.01(2)	2.00††	7.15(8)	0.85(3)	5.44(6)	6.87(3)	0.89(4)	1.16(78)	6.14/2.36
92030-02-12-02	55082.647	0.98(4)	3.05(2)	2.00††	7.50(9)	0.87(2)	4.75(4)	5.98(4)	0.90(3)	1.15(78)	6.38/2.60
92030-02-12-03	55082.581	1.01(2)	2.99(4)	2.00††	7.07(6)	0.82(4)	4.61(9)	6.15(2)	0.97(4)	1.10(78)	6.09/2.33
92030-02-12-04	55082.773	0.96(6)	3.07(3)	2.00††	7.32(6)	0.81(3)	4.28(8)	6.84(4)	0.91(2)	0.99(78)	6.20/2.62
92030-02-13-00	55088.379	1.01(1)	3.09(4)	2.00††	5.58(9)	0.88(2)	4.45(9)	6.85(5)	0.97(3)	1.06(78)	5.07/1.91
92030-02-14-00	55116.958	1.02(4)	3.09(2)	2.00††	4.52(4)	0.83(3)	3.44(4)	6.89(8)	0.94(5)	1.11(78)	4.06/1.57

† The spectral model is $wabs * (blackbody + Comptb + Gaussian)$, where N_H is fixed at a value 3.00×10^{21} cm^{-2} (Bloser et al. 2000); color temperature T_s and T_{BB} are fixed at 1.3 and 0.7 keV, respectively (see comments in the text); †† when parameter log$(A) \gg 1$, this parameter is fixed at 2.0 (see comments in the text), ††† normalization parameters of *blackbody* and *Comptb* components are in units of $10^{-2} \times L_{39}/d^2_{10}\ erg/s/kpc^2$, where L_{39} is the source luminosity in units of 10^{39} erg/s, d^2_{10} is the distance to the source in units of 10 kpc and *Gaussian* component is in units of $10^{-2} \times total\ \ photons\ cm^{-2}s^{-1}$ in line, ††††spectral fluxes (F_1/F_2) in units of $\times10^{-9}$ ergs/s/cm^2 for (3 – 10) and (10 – 60) keV energy ranges respectively.

Table 5. Comparison of parameters of atoll sources 4U 1820-30, GX 3+1[1] and 4U 1728-34[2]

Source	D, kpc	Type of donor star	Mass of donor star $M_\odot$	P_{orb}, min	i, degrees	kT_e keV	N_{comptb}, L_{39}^{soft}/D_{10}^2	kT_{BB}, keV	kT_s, keV	f	$t_{LS-HS-LS}$, days
GX 3+1	4.5[3]	A	~ 10	-	-	2.3-4.5	0.04-0.15	0.6	1.16-1.7	0.2-0.9	1000
4U 1820-30	5.8-8[4]	WD	0.07	11.46±0.04	43±9[5]	2.9-21.0	0.02-0.14	0.6	1.1-1.7	0.2-1	170
4U 1728-34	4.2-6.4[6]	?	-	-	-	2.5-15	0.02-0.09	0.6-0.7	1.3	0.5-1	15

References: (1) ST12; (2) ST11; (3) Kuulkers & van der Klis (2000); (4) Shaposhnikob & Titarchuk (2004); (5) Arons & King (1993); (6) van Paradijs (1978)

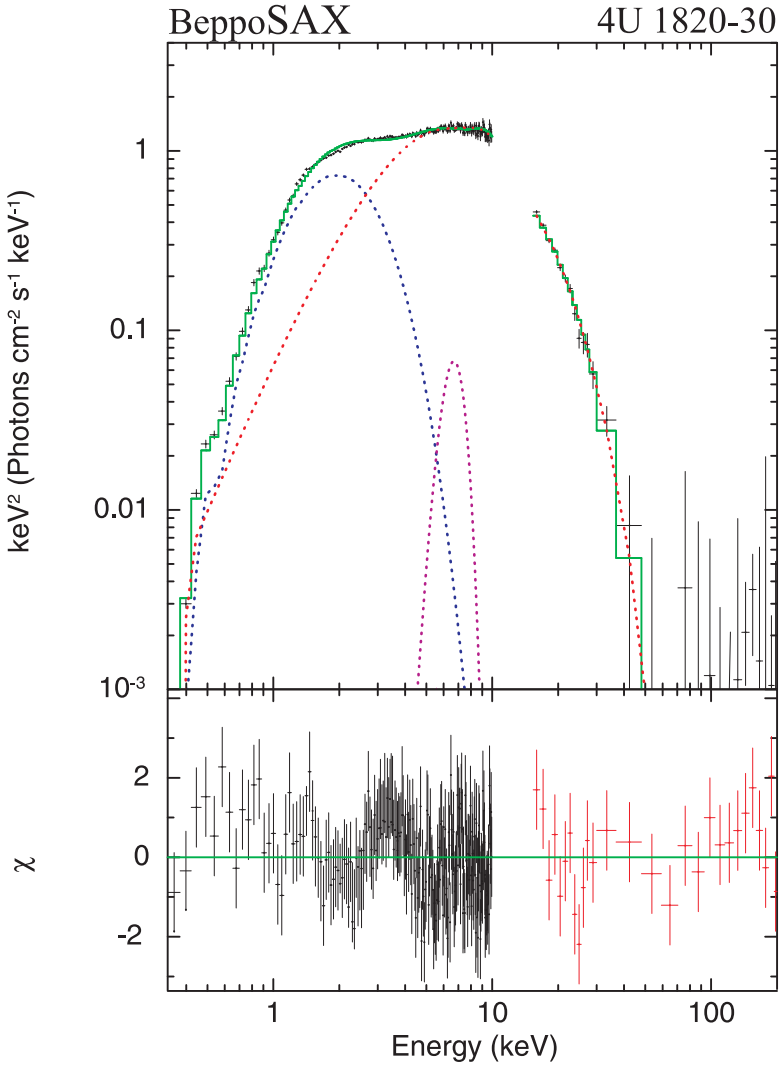

Fig. 1.— *Top* : the best-fit spectrum of 4U 1820-30 during *banana branch* events in $E*F(E)$ units using *Beppo*SAX observation 20105004 carried out on 2 October 1997. The data are presented by crosses and the best-fit spectral model *wabs*(blackbody+Comptb+Gaussian)* by green line. The model components are shown by blue, red and crimson lines for *blackbdody*, *Comptb* and *Gaussian* components respectively. *Bottom panel*: $\Delta\chi$ (reduced χ^2=1.11 for 364 d.o.f). The best-fit model parameters are $\Gamma = 2.00 \pm 0.04$, $kT_e = 3.25 \pm 0.02$ keV, $E_{line} = 6.7 \pm 0.1$ keV (see more details in Table 3).

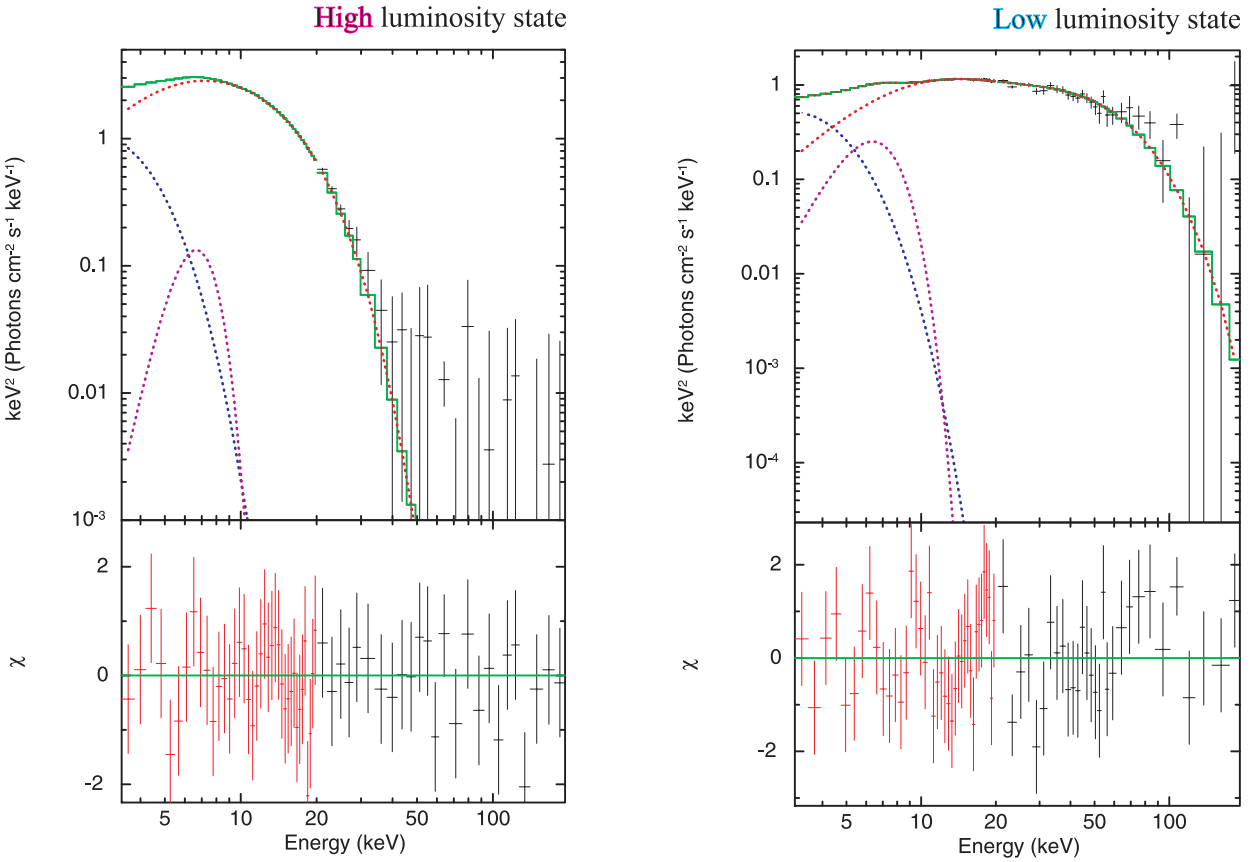

Fig. 2.— Examples of typical $E*F(E)$ spectral diagram of 4U 1820-30 during soft (*left panel*) and hard (*right panel*) state events. The best-fit *RXTE* spectra (*top* panels) using the model $wabs * (Bbody + CompTB + Gaussian)$ with $\Delta\chi$ (*bottom* panels) for the high-luminosity (*banana*) state [40017-01-11-00 observation, χ^2_{red}=1.00 for 78 d.o.f, *left panel*] and for the low-luminosity (*island*) state [94090-01-04-00 observation, χ^2_{red}=1.10 for 78 d.o.f, *right panel*]. The best-fit model parameters are Γ=1.99±0.02, kT_e=2.94±0.01 keV and E_{Gauss}=6.53±0.06 keV (for the *soft* state) and Γ=2.00±0.04, kT_e=12.54±0.09 keV and E_{Gauss}=6.35±0.04 keV (for the *hard* state) (see more details in Table 4). Blue, red and violet lines stand for *Bbody*, *CompTB* and *Gauss* components respectively.

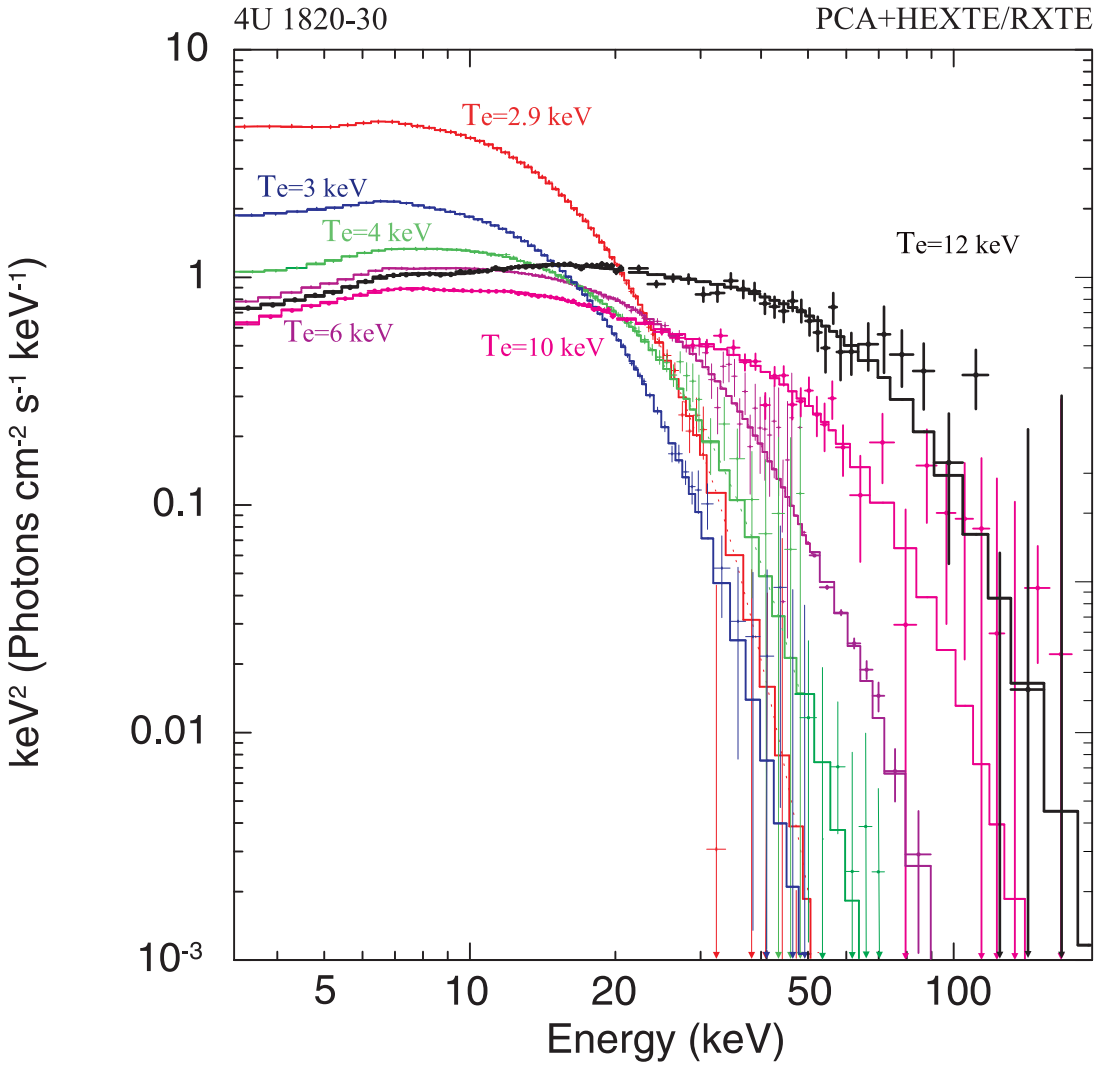

Fig. 3.— Six representative EF_E spectral diagrams which are related to different electron temperatures of TL [kT_e =2.9 keV (*red*), 3 keV (*blue*), 4 keV (*green*), 6 keV (*voilet*), 10 keV (*pink*) and 12 keV (*black*)] using the model $wabs * (Blackbody + COMPTB + Gaussian)$ for $island - banana$ state transitions of 4U 1820-30. The data are taken from *RXTE* observations 30057-01-04-01 (*red*), 70030-03-07-020 (*blue*), 70030-03-05-02 (*green*), 70030-03-05-01 (*violet*), 40017-01-24-00 (*pink*) and 94090-01-04-00 (*black*).

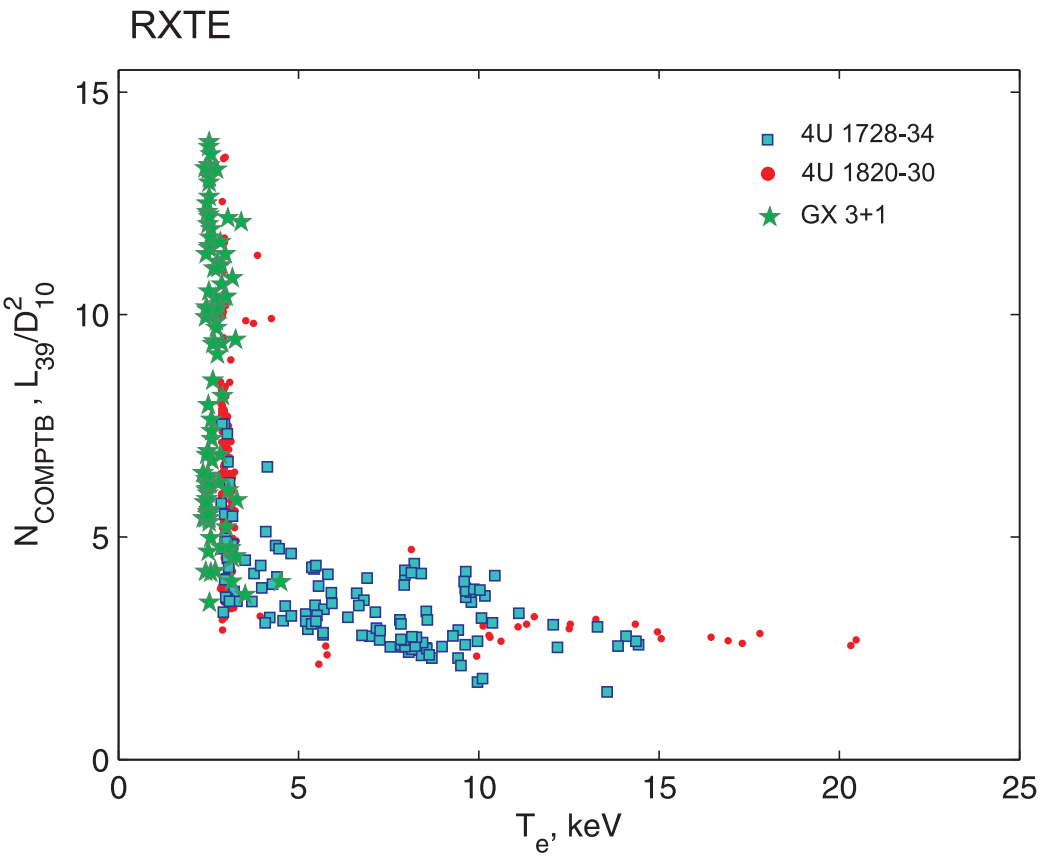

Fig. 4.— Comptb normalization measured in units of L_{39}^{soft}/D_{10}^2 versus the electron temperature kT_e (in keV) obtained using the best-fit spectral model $wabs * (blackbody + Comptb + Gaussian)$ for *atoll* sources 4U 1820-30 (*red*), GX 3+1 (*green*, taken from ST12) and 4U 1728-34 (*blue*, taken from ST11) for *RXTE* data.

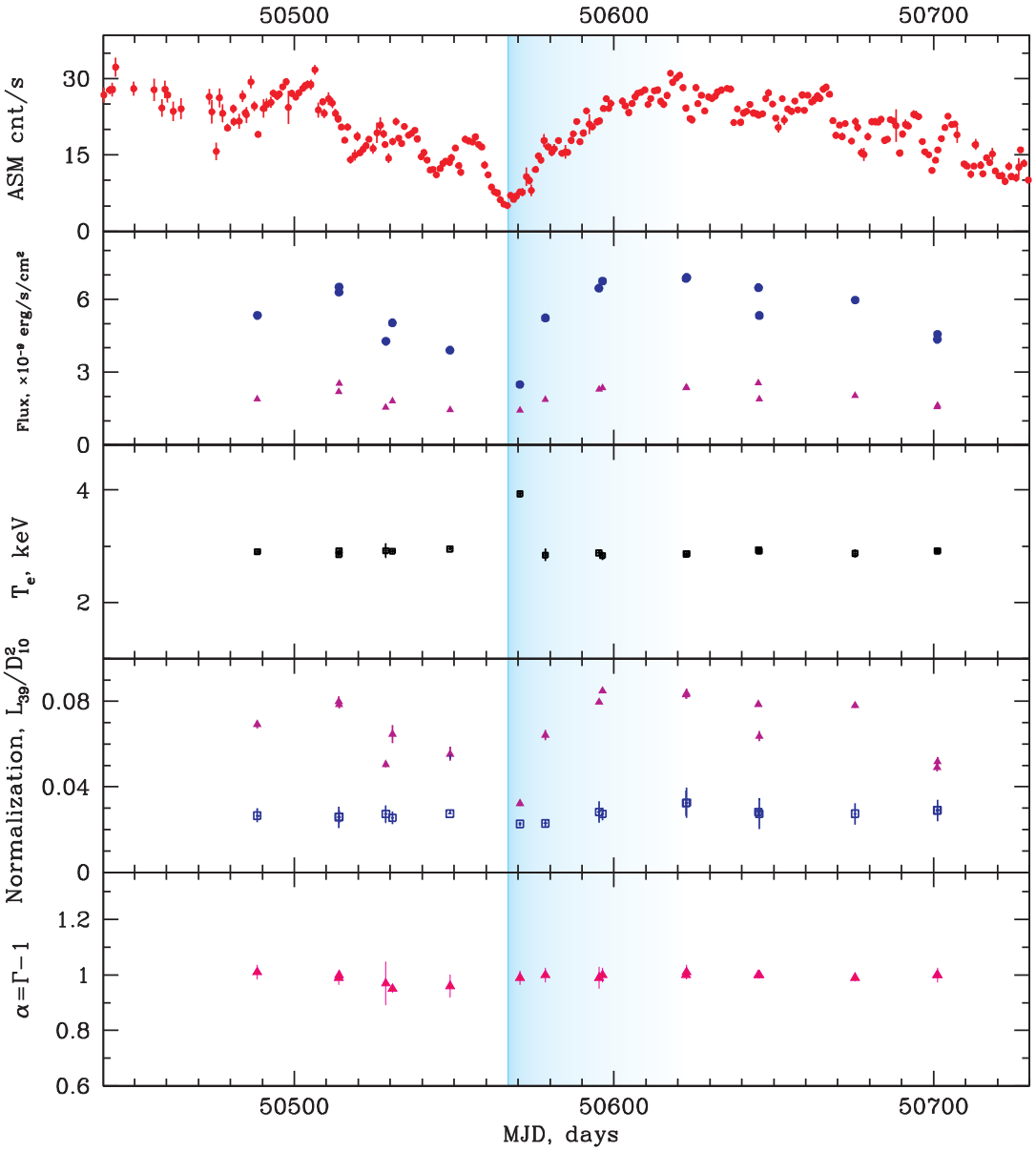

Fig. 5.— *From Top to Bottom:* Evolutions of the *RXTE*/ASM count rate, the model flux in 3-10 keV and 10-50 keV energy ranges (*blue and crimson* points respectively), the electron temperature kT_e in keV, and *Comptb* and *blackbody* normalizations (*crimson* and *blue* respectively) during 1996 – 1997 transition set (*R1* – *R2*). The rising phases of the *local* (*mild*) transitions are marked with blue vertical strips.

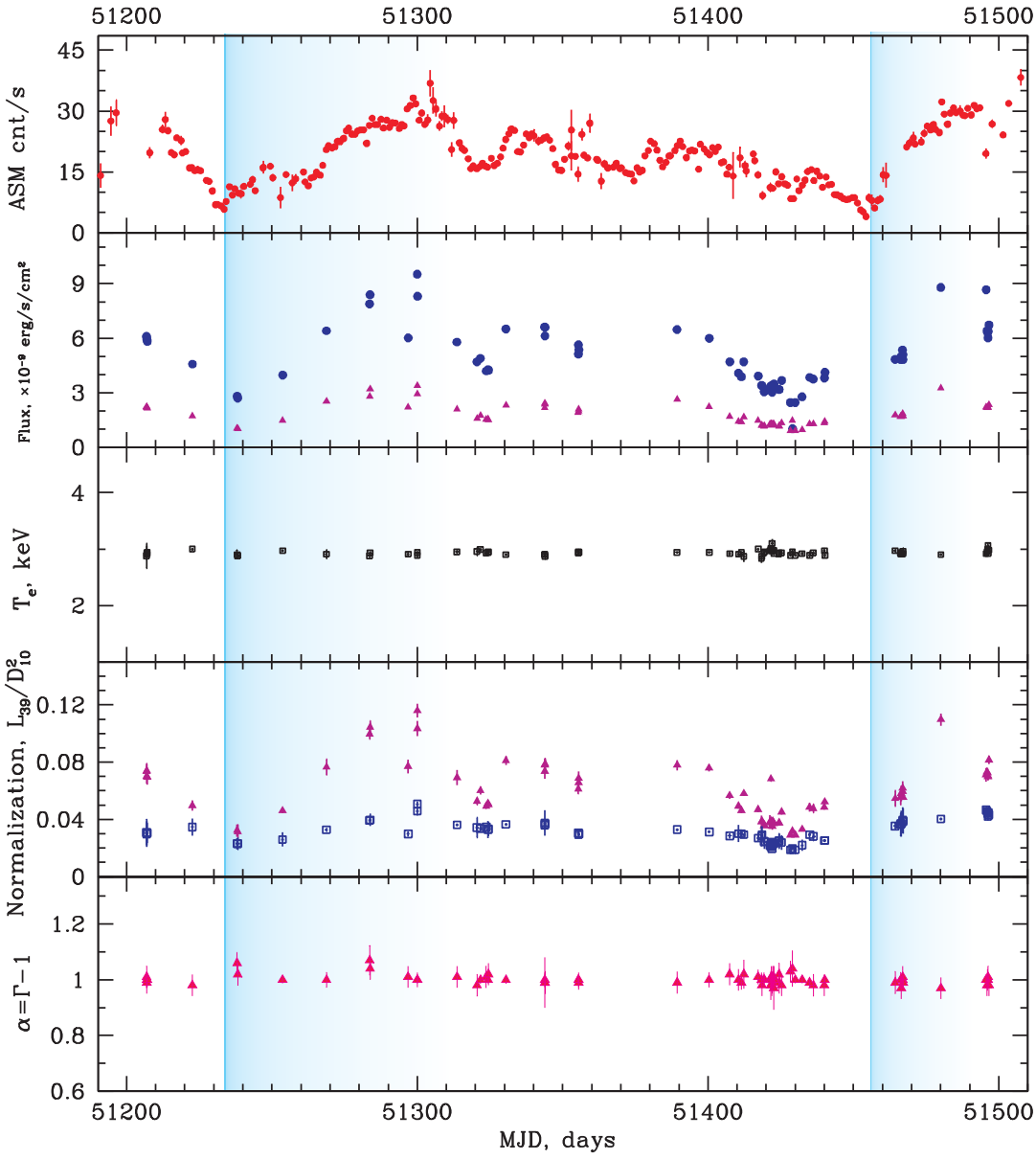

Fig. 6.— Similar to that presented in Fig. 5 but for the *RXTE* 1999 transition set *R3*.

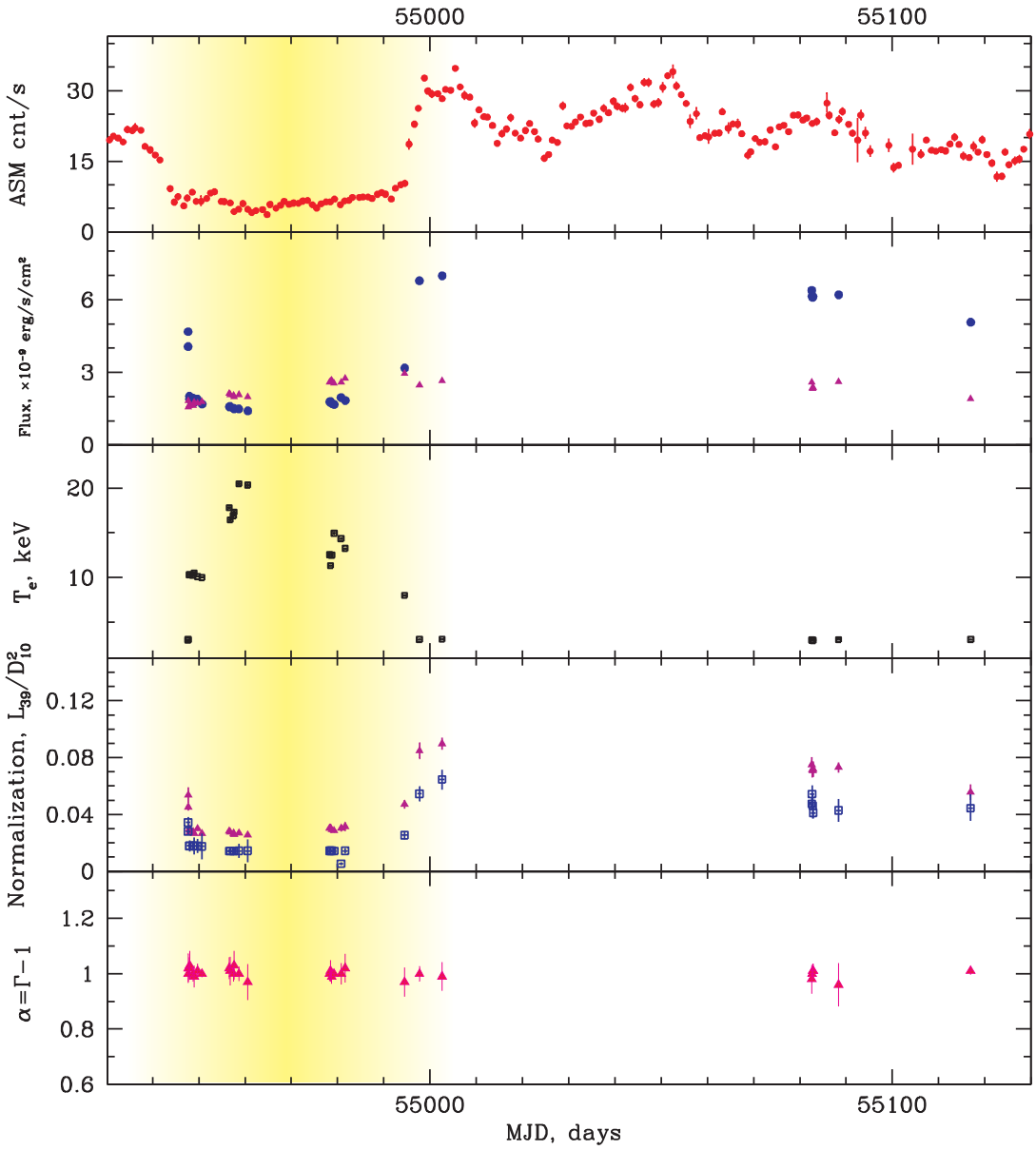

Fig. 7.— Similar to that presented in Fig. 5 but for the *RXTE* 2009 transition set *R7*. The *quasi-plateau* phases of the low luminosity state of 4U 1820-30 are marked using orange vertical strip.

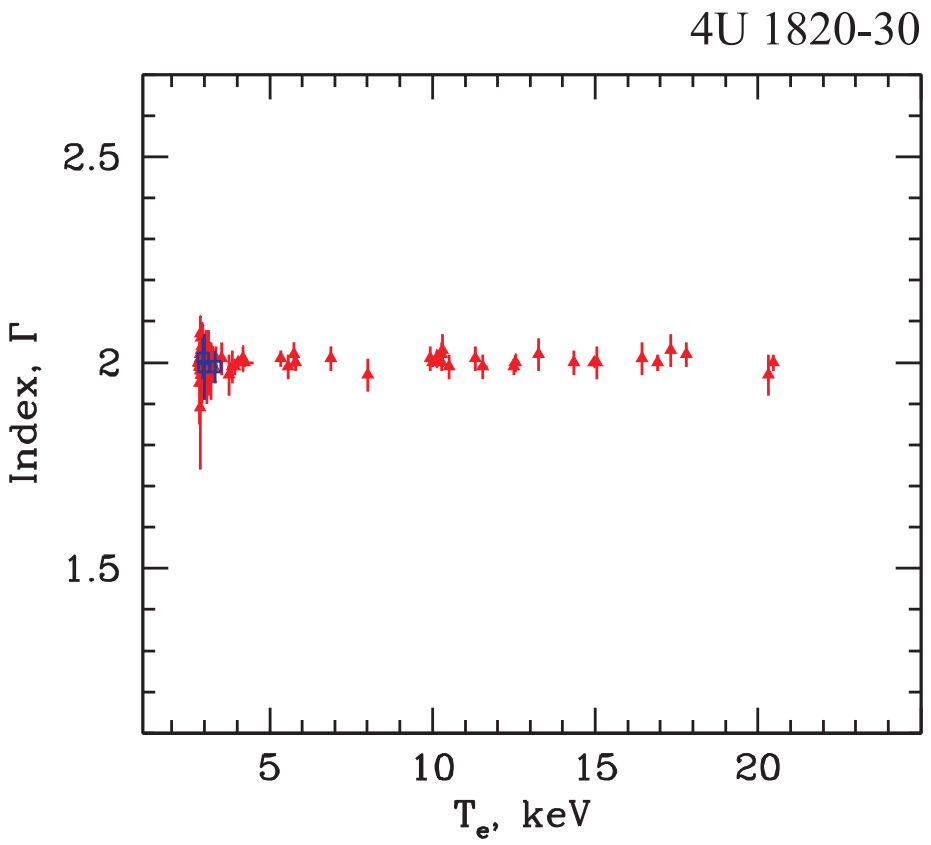

Fig. 8.— The photon index Γ plotted versus the electron temperature kT_e (in keV) in the frame of our spectral model $wabs*(blackbody+Comptb+Gaussian)$ during transition events (see Tables 3, 4). Blue and red points correspond to *Beppo*SAX and *RXTE* observations.

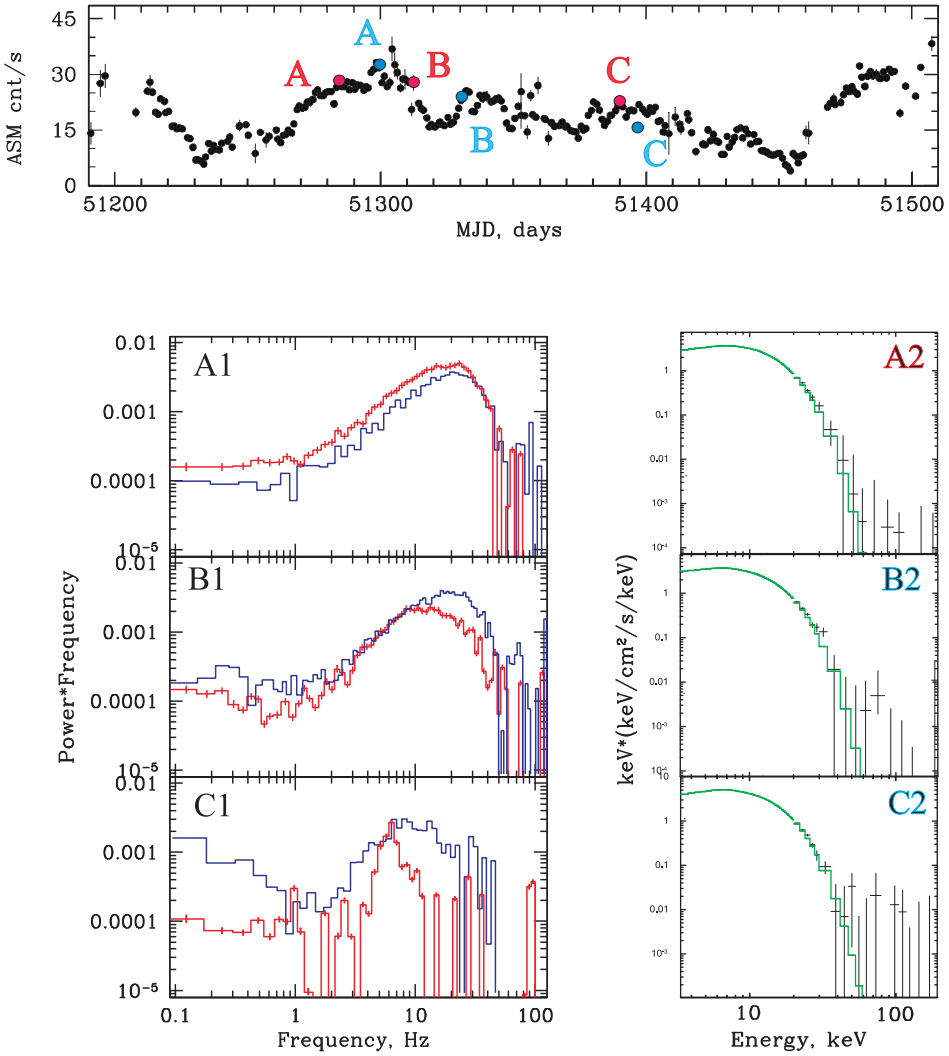

Fig. 9.— *Top*: evolution of *RXTE*/ASM count rate during the high luminosity state at $R3$ (1999) transition events. Red/blue points A, B, and C mark moments at MJD = 51283.6/51300, 51313.7/51330.5 and 51389.4/51396.26 covering different transition phases. *Bottom*: PDSs for 15-30 keV band (*left* column) are plotted along with the $E * F(E)-$diagram (*right* column) for A (*red*, top), B (*blue*, middle) and C (*blue*, bottom) points of X-ray light curve. All points are related to the *banana* state [strong broadband noise, VLFN and QPOs at ν_l ∼6 – 7 Hz (C *red*)]. The $E * F(E)-$diagrams (panels A2, B2, C2) are related to the corresponding power spectra (panels A1, B1, C1). The data are shown by black points. The electron temperature kT_e of the corresponding energy spectra of 4U 1820-30 is about 3 keV.

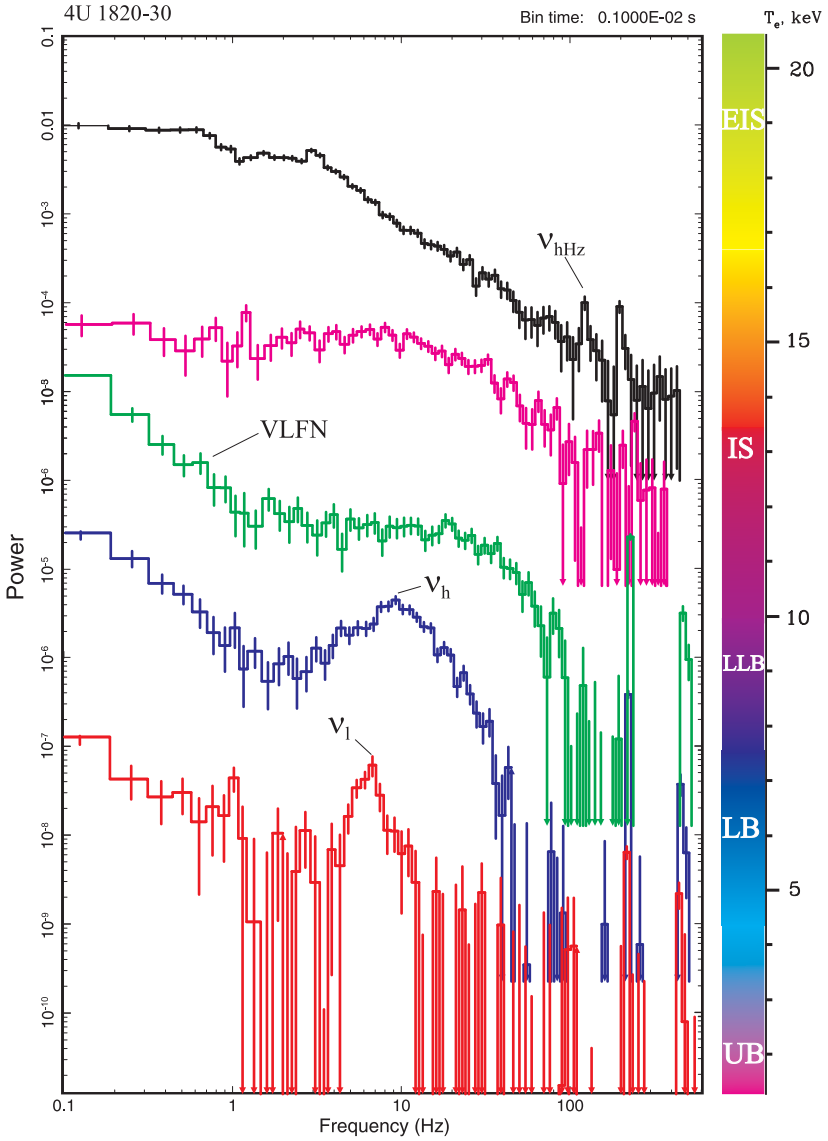

Fig. 10.— PDSs of 4U 1820-30 related to its X-ray spectral states. kT_e values (in keV) corresponding to the energy spectra are indicated at the right vertical axis. PDSs in the extreme island state (EIS), island state (IS, multiplied by factor 10^{-2} for clarity), lower left banana state (LLB, $\times 10^{-4}$), lower banana state (LB, $\times 10^{-6}$) and upper banana state (UB, $\times 10^{-8}$) are presented from *top* to *bottom*. The histograms consist of three components: VLFN (*very low frequency noise* in *banana* states), the peaked noise component, low-frequency QPOs are fit by Lorentzians (ν_l, ν_h) and high frequency QPO (ν_{hHz}).

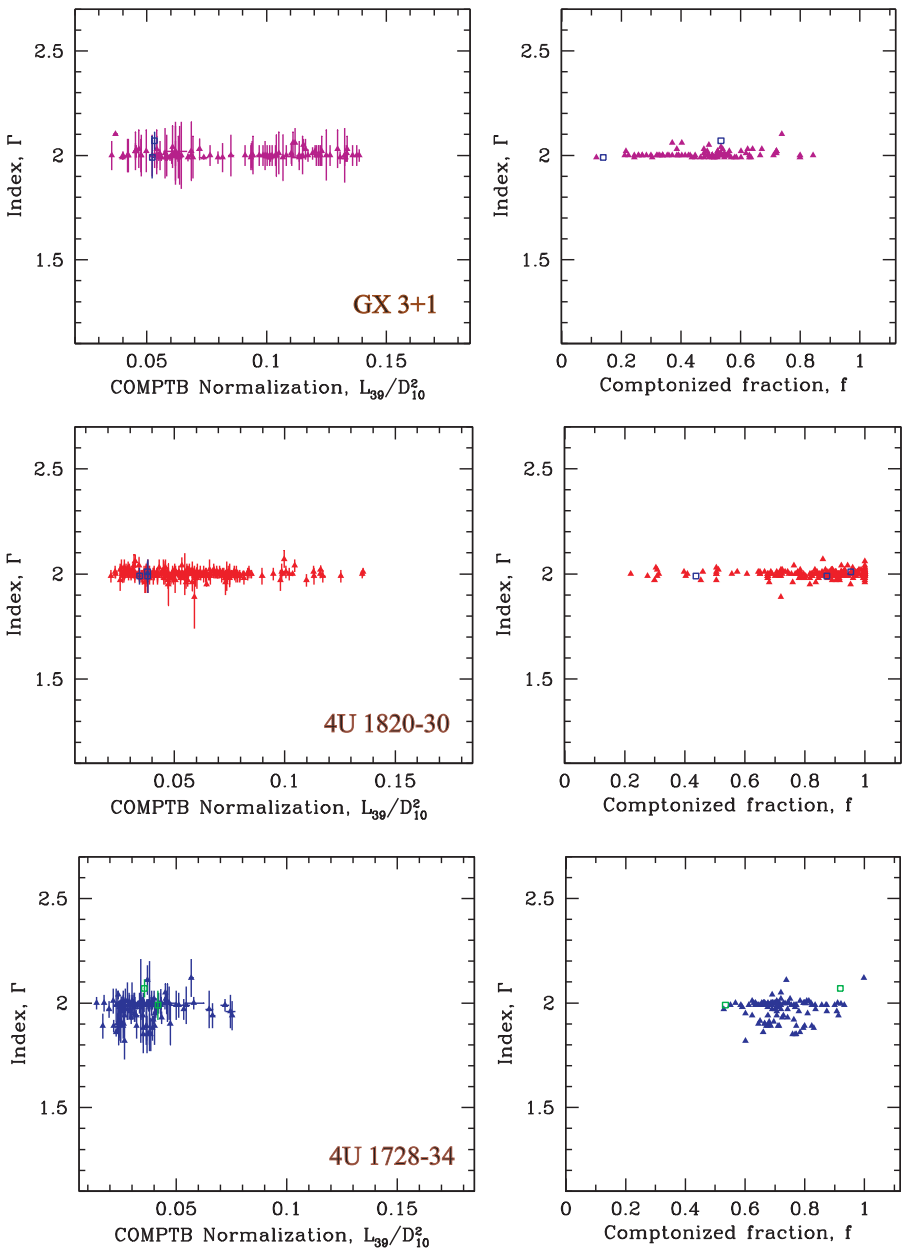

Fig. 11.— *From Top to Bottom:* Plots Γ vs Comptb Normalization (*left column*) and vs Comptonized fraction f (*right column*) for GX 3+1 (*top*), 4U 1820-30 (*middle*) and 4U 1728-34 (*bottom*) obtained using the $wabs * (blackbody + Comptb + Gaussian)$ model. On the *top* panels *crimson* and *blue* points are for GX 3+1 taken from ST12 and on the middle panels for 4U 1820-30 *red* and *blue* points correspond to *RXTE* and *Beppo*SAX data respectively (current study). On the *bottom* panels *blue* and *green* points correspond to *RXTE* and *Beppo*SAX data respectively for 4U 1728-34 (data taken from ST11).

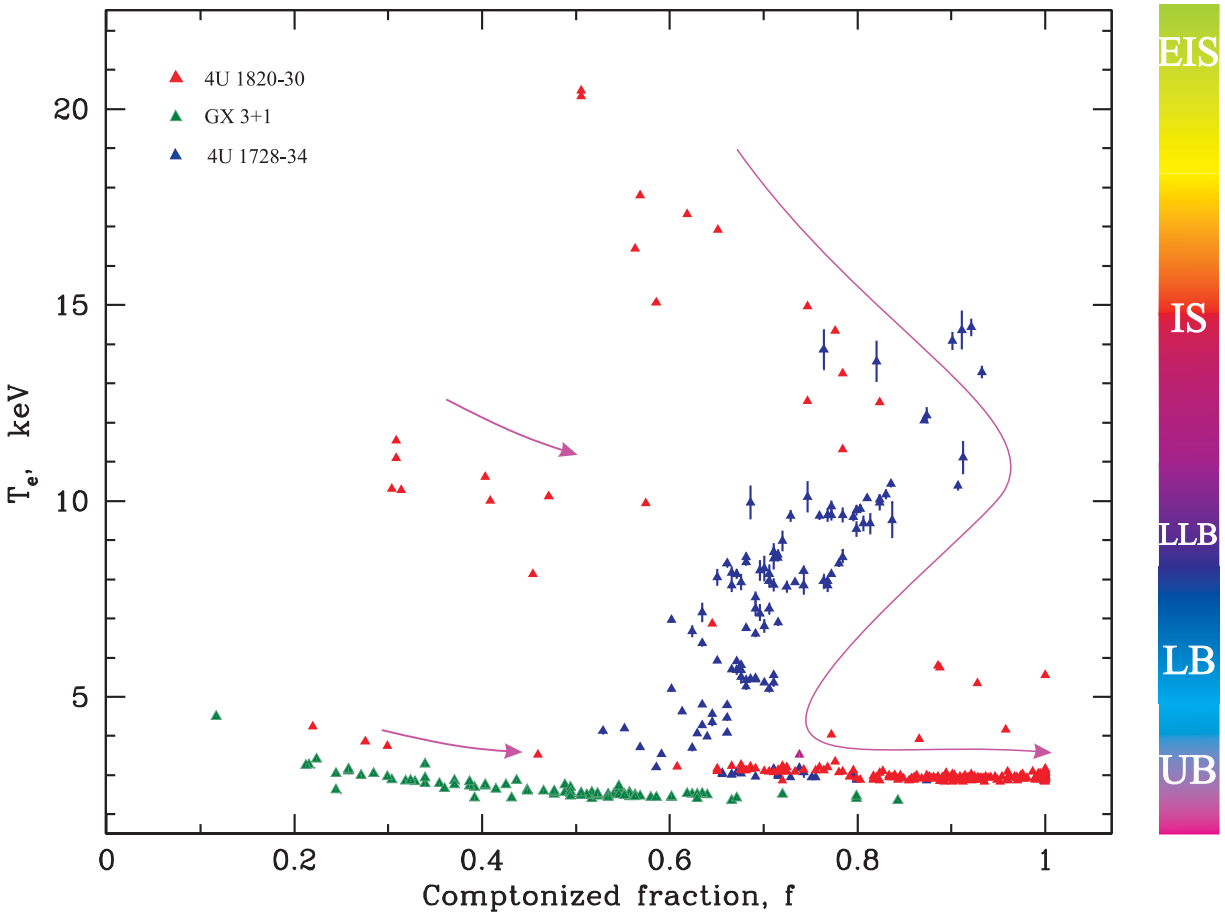

Fig. 12.— kT_e (in keV) plotted versus illumination fraction f for 4U 1820-30, GX 3+1 (taken from ST12) and 4U 1728-34 (taken from ST11) during spectral state transitions obtained using the *wabs* $*$ (*blackbody* + *Comptb* + *Gaussian*) model. *Red, green* and *blue* points correspond to *RXTE* observations of 4U 1820-30, GX 3+1 and 4U 1728-34 respectively. The *bended arrows* are related to an increase of mass accretion rate. On the right-hand side of the Figure we show a sequence of CCD states (EIS – extreme island state, IS – island state, LLB – lower left banana state, LB – lower banana state and UB – upper banana state) which are listed according to the standard *atoll*−Z scheme (Hasinger & van der Klis 1989). One can see that kT_e is directly related to the sequence of CCD stages.

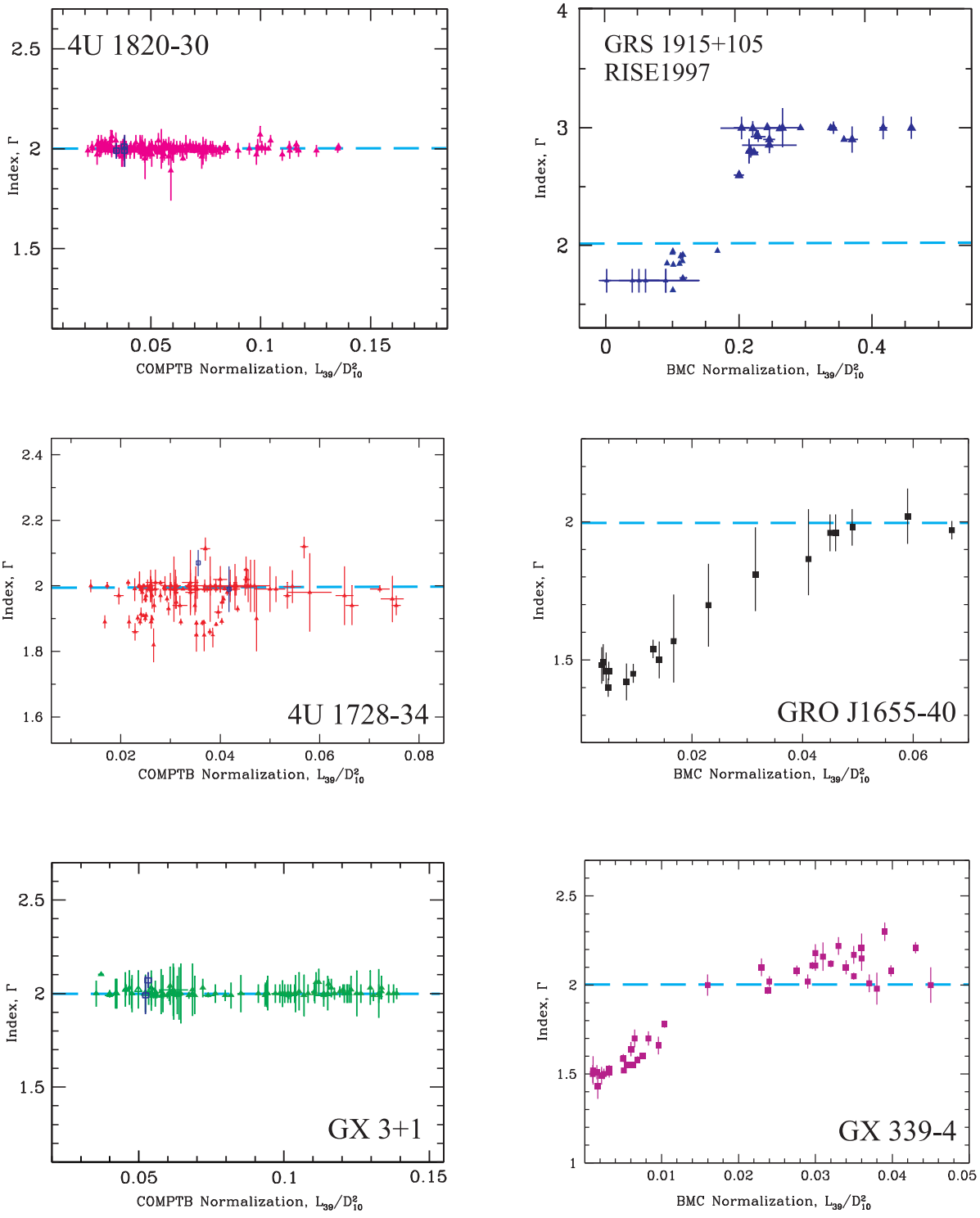

Fig. 13.— Examples of diagrams of the photon index Γ versus the COMPTB normalization (proportional to mass accretion rate) for BH sources [right column, GRS 1915+105 (TS09), GRO J1655-40 (ST08) and GX 339-4 (ST08)] along with *atoll* NS sources [left column, 4U 1820-30, 4U 1728-34 (ST11) and GX 3+1 (ST12)]. For all plots the *RXTE* data were used along with *Beppo*SAX data (indicated by blue points on the *left* column). One can see a noticeable change of Γ followed by the saturation plateau for BHs as for NSs the index only slightly varies about 2. The level for $\Gamma = 2$ is indicated by blue dashed line.